minerals

MDPI

Article

Genesis of the Caijiagou Gold Deposit in the West Qinling Orogen, China: Constraints from In Situ Trace Element Analysis, Sulfur Isotopes of Sulfide, and Apatite U–Pb Dating

Xin Song [1,2,3], Wei Li [4,5,*], Chao Wang [1,2,3], Zheng Li [1,2,3], Junxing Ma [1,2,3] and Shengping Li [1,2,3]

1 Gansu Provincial Key Laboratory of Mineral Resources Exploration, Lanzhou 730000, China; aisxlg521@163.com (X.S.); 15378818338@163.com (C.W.); boyutao4271@163.com (Z.L.); 15009386491@163.com (J.M.); 13919667719@163.com (S.L.)
2 The First Institute of Geological and Mineral Exploration of Gansu Provincial Bureau of Geology and Mineral Resources, Tianshui 741020, China
3 Gansu Provincial Exploration Research Center of Comprehensive Exploration and Utilization and Protection of Mineral Resources, Tianshui 741020, China
4 Xi'an Mineral Resources Survey, China Geological Survey, Xi'an 710100, China
5 Technology Innovation Center for Gold Ore Exploration, China Geological Survey, Xi'an 710100, China
* Correspondence: lww1273494112@163.com

Abstract

The newly discovered Caijiagou gold deposit is hosted in metasedimentary rocks of the Silurian Taiyangsi Formation in the West Qinling Orogen (WQO), central China. Three mineralization stages are recognized: (1) the quartz–sericite–pyrite stage (Stage I), characterized by fine-grained, disseminated pyrite (Py1) and arsenopyrite (Apy1) with trace amounts of native gold; (2) the main ore-stage, the quartz–polymetallic sulfide–ankerite stage (Stage II), which contains coarse-grained euhedral pyrite (Py2) and arsenopyrite (Apy2) intergrown with ankerite and native gold; and (3) the post-ore calcite stage (Stage III), which is barren. Hydrothermal alteration assemblages include silicification, sericitization, pyritization, and carbonatization. In situ trace element analyses show that gold is mainly hosted in Py2 (avg. 2.86 ppm Au) and Apy2 (avg. 1.95 ppm Au), with consistently low Co/Ni ratios (<0.6) in ore-stage sulfides, supporting a metamorphic fluid origin. Sulfur isotope values ($\delta^{34}S$ = +6.47‰ to +11.96‰) point to sulfur derived from thermochemical reduction of marine sulfate. Apatite from the main ore stage (Stage II) yields a U–Pb lower intercept age of 237 ± 4.3 Ma (MSWD = 0.89), placing the mineralization in the Middle Triassic (Indosinian orogeny). These results are consistent with a sediment-hosted orogenic gold model, and the geochemical and geochronological signatures provide insights into the ore-forming process and regional metallogeny of the WQO.

Keywords: Caijiagou gold deposit; orogenic gold; trace element; sulfur isotope; apatite U–Pb dating

Check for updates

Academic Editor: Bernhard Schulz

Received: 27 June 2026
Revised: 24 July 2026
Accepted: 29 July 2026
Published: 30 July 2026

Copyright: © 2026 by the authors. Licensee MDPI, Basel, Switzerland. This article is an open access article distributed under the terms and conditions of the Creative Commons Attribution (CC BY) license.

1. Introduction

The Qinling orogenic belt is a key component of the Central Orogenic System of the Chinese continent. Since the Neoproterozoic, it has undergone polycyclic, multiphase, and multi-regime orogenesis, resulting in a tectonic framework of "two sutures and three blocks". The two sutures are the Shangdan and Mianlüe suture zones, and the three blocks are the southern margin of the North China Block, the Qinling microblock, and the northern margin of the South China Block (Figure 1a). This framework is the product of multiple

episodes of ocean-basin spreading and subduction, ocean–continent subduction orogeny, continent–continent collisional orogeny, and superimposed intracontinental orogeny that involved these blocks, which together make the Qinling orogenic belt a typical composite continental orogen [1–4]. The Fengxian–Taibai fault zone demarcates the West Qinling Orogen (WQO) from the East Qinling orogenic belt, with the former located in a transitional zone where major terranes and orogenic belts of the Chinese continent converge and interact (Figure 1b) [2,5,6]. During the Triassic to Middle Jurassic (250–170 Ma), the WQO experienced subduction and closure of the Paleo-Tethyan Mianlüe oceanic basin. The South China Block finally collided with the West Qinling microterrane along the A'nyemaqen–Mianlüe suture zone, followed by intracontinental deformation characterized by large-scale thrust napping, compression, rotation, uplift, and plutonic intrusion of magmatic activity, culminating in intense tectonic–magmatic–metallogenic events [7–13]. Owing to the migration pathways provided by structural deformation, combined with abundant ore-forming materials derived from intense magmatic activity and metamorphic strata, these materials eventually precipitated and enriched at favorable sites, giving rise to a series of gold deposits in the West Qinling area, including the Zaozigou, Zhaishang, Liba, Huayagou, Xiangtanzi, Jinchanggou, and Baguamiao deposits [4,9,14–16]. As a result, the WQO is increasingly recognized as the second-largest gold base in China [17], exhibiting substantial exploration potential. Regarding the genetic mechanisms of Indosinian gold deposits in the WQO, most studies have suggested that they are orogenic gold deposits of predominantly metamorphic hydrothermal origin [2,18,19]. However, recent research indicates that many of these gold deposits are located near intrusions and are closely associated with dykes [16,20–22], and their ore-forming materials show multiple fluid sources including meteoric water [23], metamorphic fluids derived from dewatering of supracrustal rocks [17,24,25], magmatic hydrothermal fluids [20–22,26,27], and lower crustal or mantle fluids [4,28–32]. Consequently, the sources of fluids, sulfur, gold, and other metals in these gold deposits remain controversial.

The Chaijiazhuang–Taiyangsi Au-Ag-Pb-Zn-Cu polymetallic metallogenic belt is one of the important ore belts in the WQO [3,33,34]. Regionally, numerous deposits have been discovered, including the Xiangtanzi gold deposit and the Liushaogou silver–polymetallic deposit, among which gold is the dominant mineral commodity [35–37]. Gold mineralization in this belt is confined to particular lithological units and structures, and is closely associated with magmatic activity [4,15,38–40]. In recent years, a new gold occurrence has been identified at Caijiagou, adjacent to the Liushaogou area, with Au grades ranging from 1.45 to 5.00 g/t. Some ore bodies are relatively thick (0.86–2.68 m), indicating considerable potential. However, its ore-forming mechanism remains unknown, and the sources of ore-forming fluids as well as the mineralization age have not been effectively constrained. Based solely on its proximity to the Xiangtanzi and Liushaogou gold deposits, it is tentatively inferred to be an Indosinian orogenic gold deposit. Therefore, the Caijiagou gold occurrence warrants further investigation. The present study aims to characterize the mineralogical and geochemical features of sulfides from different mineralization stages at the Caijiagou deposit, constrain the source of ore-forming fluids using in situ sulfur isotope and trace element data of pyrite and arsenopyrite, determine the timing of mineralization via apatite U–Pb dating, and establish a genetic model for the Caijiagou gold deposit within the tectonic framework of the WQO.

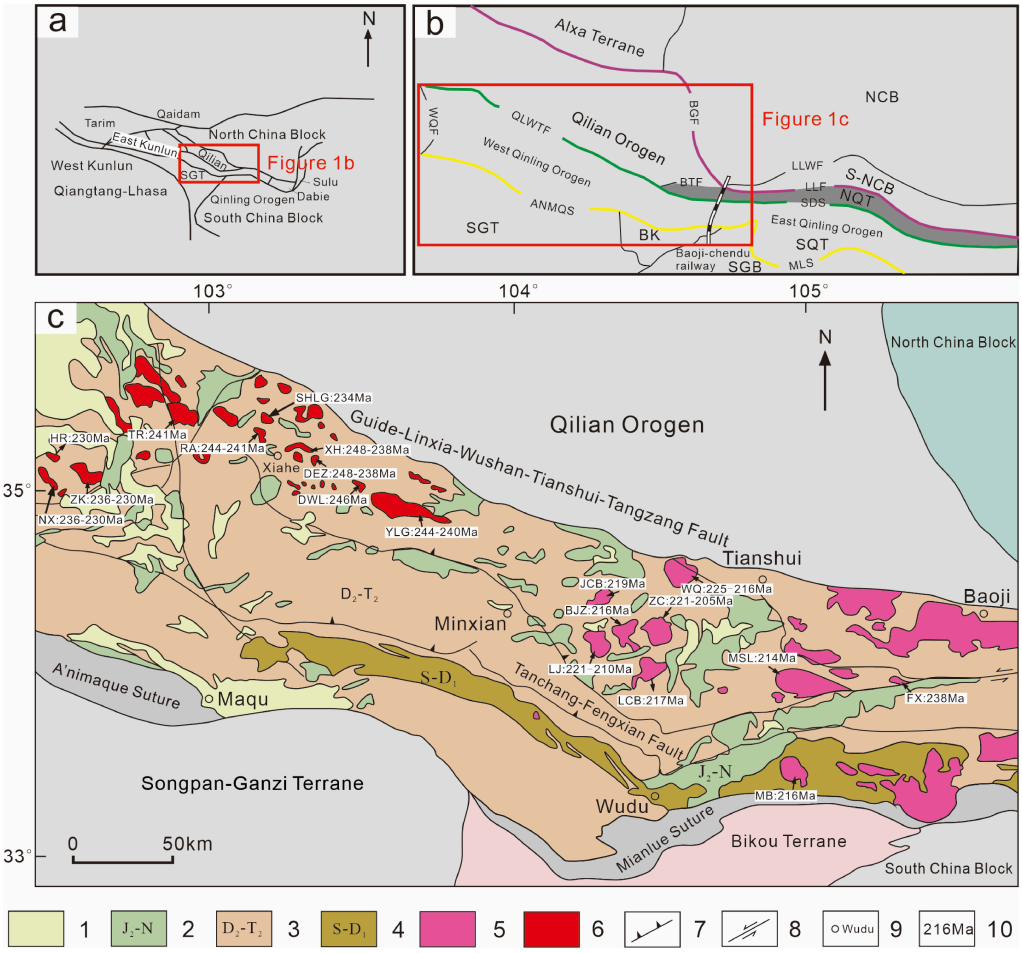


Figure 1. Tectonic division map and distribution of major magmatic rocks in the West Qinling Orogen [17]. (**a**) Major tectonic domains of China and the location of the Qinling Orogen. (**b**) Tectonic units and major boundaries of the Qinling Orogen. (**c**) Simplified geological map of the West Qinling Orogen, showing the Triassic intrusions. 1. Quaternary System, 2. Middle Jurassic to Neogene System, 3. Middle Devonian to Middle Triassic System, 4. Silurian to Lower Devonian System, 5. Late Triassic magmatic rocks, 6. Middle Triassic magmatic rocks, 7. thrust fault zone, 8. sinistral strike-slip fault, 9. city names, 10. magmatic age.

2. Regional Geology and Deposit Geology

2.1. Regional Geology

The WQO is located between several tectonic units. Its northern boundary is the Guide–Linxia–Wushan–Tianshui–Tangzang Fault, which separates it from the Qilian Orogen. The southern boundary is the A'nyemaqen–Mianlue suture zone, bordering the Songpan–Ganzi Orogen. To the east, the Fengxian–Taibai Fault (approximately marked by the Baoji–Chengdu Railway) connects it with the East Qinling Orogen, whereas to the west, the Wenquan–Wahongshan Fault delimits it from the East Kunlun Terrane and the Qaidam Block (Figure 1) [16,18,22,32,36,41,42]. Situated between the North China and Yangtze Blocks, the Qinling Orogenic Belt is conventionally separated by the Shangdan suture zone into the North Qinling Orogen and South Qinling Orogen [10,12]. This suture represents the closure of the Proto-Tethyan Shangdan Ocean during the Late Devonian. The southern boundary of the South Qinling Orogen is defined by the Mianlüe suture zone, formed through subduction and closure of the Paleo-Tethyan Mianlüe Ocean from the Late Permian to Early Triassic [1,4,15,18,43,44].

The study area is located in the southeastern part of Gansu Province, eastern part of the WQO (Figure 1c). Tectonically, it lies at the junction between the Shangdan ophiolitic mélange belt and the southern margin of the North Qinling continental marginal basin [3,4,33]. In terms of metallogenic affiliation, it belongs to the North Qinling Chaijiazhuang–Taiyangsi Au-Ag-Pb-Zn-Cu polymetallic sub-belt, which is part of the Changba–Yeshuihe Pb-Zn-Au-Ag metallogenic belt [4,45]. Intense volcanic activity in the area provided the material basis for the mineralization of elements such as gold, silver, and lead [4,15,17,38,46,47]. During the Indosinian orogeny, widespread intermediate–acidic magmatic intrusions supplied the thermal driving force for the activation, migration, and enrichment of ore-forming materials [35,38,44,48]. The area shows evidence of complex tectonic activity with faults providing favorable pathways and space for mineralization.

The exposed strata in the region include the Paleoproterozoic Qinling Group, the Silurian Taiyangsi Formation, the Ordovician Liziyuan Group and Chenjiahe Group, the Devonian Xihanshui Group, Shujiaba Group, and Dacaotan Group, and the Triassic Huari Formation (Figure 1c) [33,34,36]. These strata were intensely folded and faulted during the Permian–Triassic subduction and closure of the Paleo-Tethyan Mianlüe Ocean and subsequent continent–continent collision [49,50]. As a result, they generally strike northwest to nearly east–west, largely consistent with the orientation of regional fault lines (Figure 1c), and occur mostly as tectonically controlled structural slices [8,17,48,51]. Among these, the Devonian formations constitute the primary ore-hosting strata for known gold mineralization in the region [52,53].

Regionally, the structural framework is roughly east–west, with pervasive faulting and folding. Four fault sets are recognized [11,33,34,36,51]: (1) early major east–west faults (e.g., Yuanjiaping and Taiyangsi) with multi-stage activity; (2) secondary east–west compressional reverse faults, mostly south-dipping, developed later, and serving as the primary ore-hosting structures; (3) northwest- and northeast-trending compressional-shear reverse faults, commonly mineralized and altered, representing the most important ore-bearing structures; and (4) late north–south-trending faults that cut across earlier faults and strata. The folds are small-scale.

The area has experienced multiphase magmatic activity, with igneous rocks exposed from the Caledonian to the Indosinian (Figure 1c) [12,17,22,43,44,46]. Intense pre-Caledonian magmatism laid the material foundation for ore enrichment in various deposits [10], whereas later magmatism produced abundant intermediate-acidic dykes [46]. The heat from the latter provided the thermal driving force for metal mobilization, ore-fluid migration, and concentration of useful components [35,46,54]. Three major plutons are exposed in the region: the Taibai, Tianzishan, and Moshan'gou plutons. The Tianzishan pluton is the largest, with the Tianzishan and Taibai plutons having roughly east–west-trending long axes, and the Moshan'gou pluton showing a nearly north–south trend [5,54–58].

Intermediate-acidic dykes are widely developed in the area, consisting mainly of diorite (diorite porphyrite), quartz diorite (quartz diorite porphyrite), and granite porphyry [33,34]. Their geometry is predominantly controlled by northwest- and northeast-trending faults, and to a lesser extent by east–west-trending faults. The dykes are generally several to several tens of meters wide and typically several tens of meters long, whereas north–south-trending dykes are relatively rare. Gold mineralization in the area is closely associated with these intermediate-acidic dykes [4,17,38,39,46].

2.2. Deposit Geology

The Caijiagou gold deposit lies in Liangdang County, Gansu Province, in the eastern part of the WQO (Figure 1c). To the north are the Shangdan suture zone and the Yuanjiaping ductile shear zone. The exposed strata in the mining area are simple: all rocks belong

to the Silurian Taiyangsi Formation ($S_{3–4}t$), mainly composed of quartz schist (Figure 2a). The rocks are so intensively deformed that the original bedding (S_0) has been largely transposed and replaced by pervasive foliation and even mylonitization. This unit is a low- to medium-grade metamorphosed clastic sequence. A notable feature is its generally high quartz content. From the lithological assemblage, the protoliths were likely mature quartz sandstone, fine-grained quartz sandstone, and argillaceous quartz siltstone, pointing to a stable depositional setting. Regional tectonic data further suggest a passive continental margin environment for the Taiyangsi Formation. Based on lithological changes, the formation splits into three members: the first ($S_{3–4}t^1$), second ($S_{3–4}t^2$), and third ($S_{3–4}t^3$). Of these, the second member ($S_{3–4}t^2$) is the main ore-host horizon in the area—all five discovered ore bodies occur within it (Figure 2a).

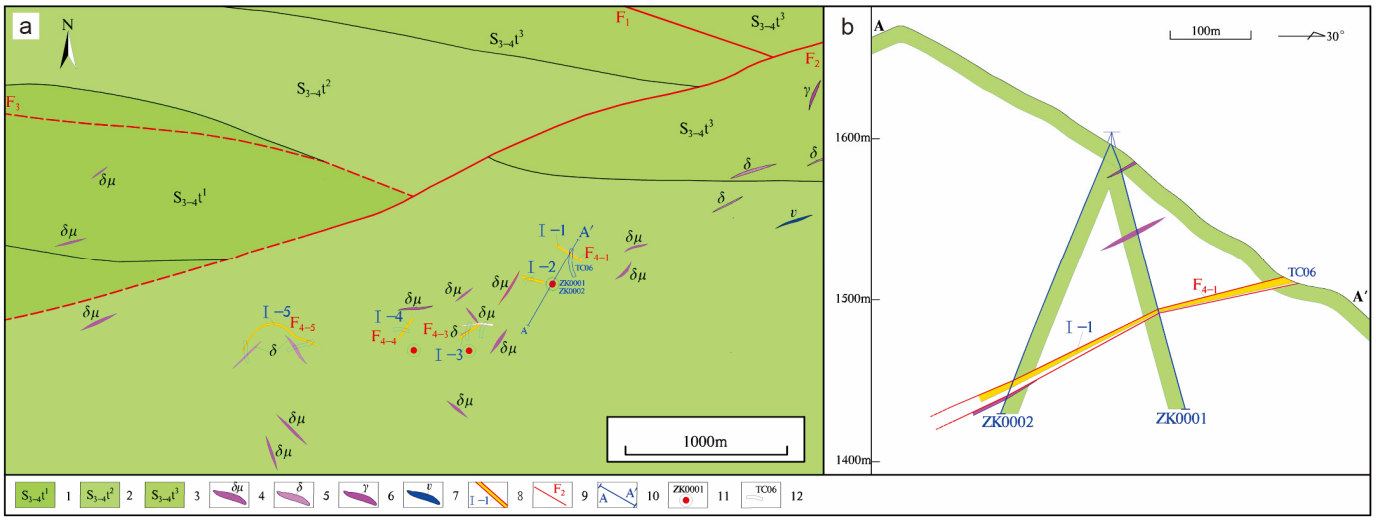


Figure 2. Geology of the study (**a**) and exploration-line cross-section map (**b**) of the Caijiagou ore district. 1. Member 1 of the Taiyangsi Formation, 2. Member 2 of the Taiyangsi Formation, 3. Member 3 of the Taiyangsi Formation, 4. diorite porphyrite dyke, 5. diorite dyke, 6. granite dyke, 7. Gabbro dyke, 8. gold orebody (location and designation), 9. fault (location and designation), 10. exploration line (location and designation), 11. drill hole (location and designation), 12. trench (location and designation).

The mining area contains a well-developed fault system. Multiphase tectonism created pathways and traps for gold-bearing hydrothermal fluids. The regional F2 fault, trending northeast (Figure 2a), is a compressional-shear structure with associated acidic dykes. Secondary faults along its flanks—trending east–west, northeast, and northwest—serve as the main ore-hosting and ore-controlling structures. The F1 and F3 faults are east–west reverse faults with compressional breccia zones (Figure 2a). The F4 fault zone, composed of multiple fault sets and generally dipping south, hosts limonitization, pyritization, and silicification. This zone is the primary ore-hosting structure in the area, controlling all five ore bodies and two mineralized bodies.

In the mining area, diorite porphyrite dikes, diorite dikes, and quartz veins occur, mainly within the second member of the Taiyangsi Formation ($S_{3–4}t^2$) (Figure 2a). Controlled by faults, the dikes trend roughly east–west or northwest, generally 0.50–11.20 m wide and 20–180 m long. The diorite (porphyrite) dikes are closely associated with gold mineralization and serve as an indirect exploration guide. The diorite porphyrite dikes show a relict porphyritic texture and massive structure, with phenocrysts (5%–12%) of altered plagioclase (completely carbonatized and chloritized) and corroded quartz, and a matrix (78%–95%) of plagioclase (strongly carbonatized and sericitized) and hornblende (carbonatized and chloritized). The diorite dikes have a subhedral granular texture and

massive structure, consisting of plagioclase (strongly epidotized, chloritized, and weakly argillized), hornblende (pleochroic), and pyroxene (carbonatized and chloritized), all intensely altered.

The mineralized zone in the area trends roughly east–west, measuring 3400 m long and 20–50 m wide. It contains one gold–polymetallic ore body (I-1), two gold ore bodies (I-4, I-5), two low-grade gold ore bodies (I-2, I-3), and three gold-mineralized bodies, all hosted in the second member of the Taiyangsi Formation (Figure 2a). The gold (mineralized) bodies are controlled by gently dipping faults trending east–west, northwest, and northeast. They are vein-like, generally dipping south at 5–32°, but locally steepening to 60–70° (Figures 2b and 3a). Individual ore bodies are 40–210 m long and 0.86–2.68 m thick, with Au grades of 1.45–5.00 g/t. Some bodies swell and pinch, with the thicker parts being more strongly mineralized. Surface alteration is mainly limonitization and hematitization, along with pyritization, galenization, and malachitization. At depth, pyritization and silicification dominate, with minor galenization; pyrite occurs unevenly as fine veinlets and small clots.

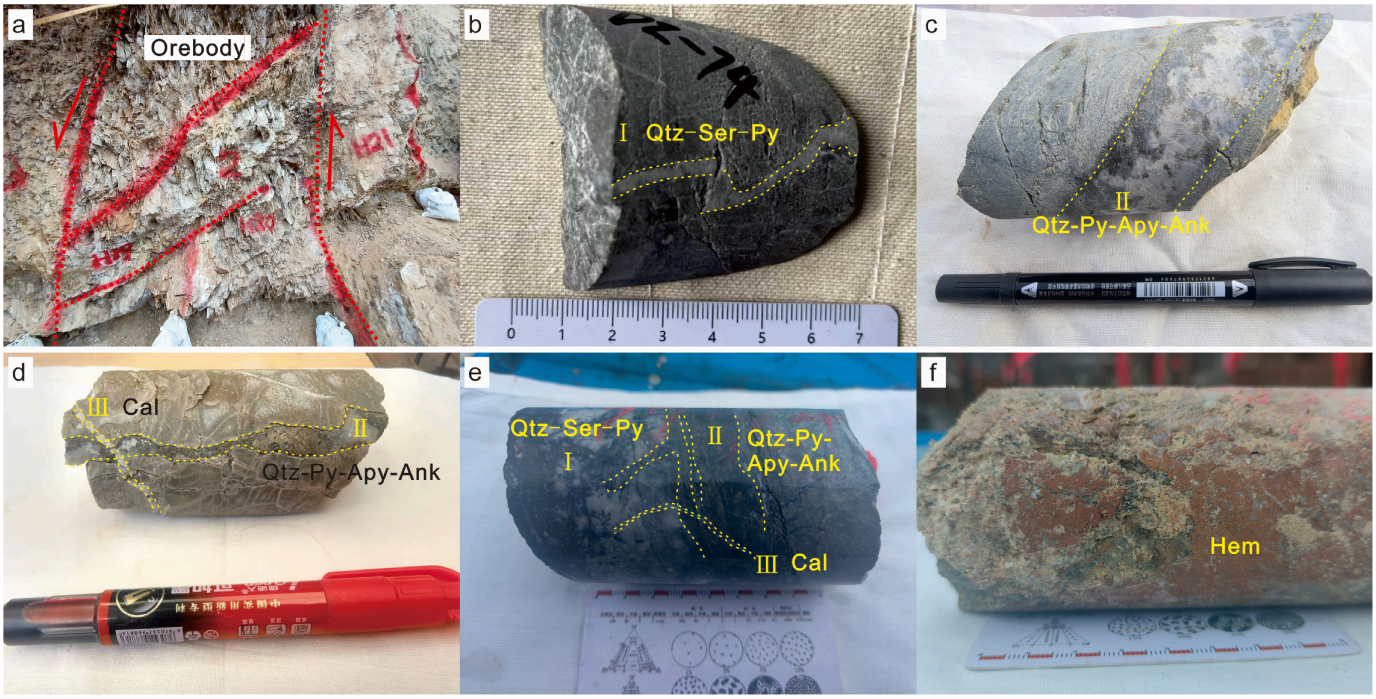


Figure 3. Field photographs of orebodies and drill-core ores. (**a**) Subvertical orebody exposed in the field. (**b**–**e**) Primary ore from boreholes. (**f**) Shallow oxidized ore. Qtz—quartz, Ser—sericite, Py—pyrite, Apy—arsenopyrite, Ank—ankerite, Cal—calcite, Hem—hematite.

3. Petrology and Petrography of the Ore Rocks

The Caijiagou gold deposit is of the tectonically-altered rock type (Figure 3). The ore has a granoblastic texture, subordinately lepidogranoblastic texture, and massive structure, with a subordinate schistose structure.

The natural ore types include oxidized ore, mixed ore, and sulfide ore. The oxidized zone roughly extends from the surface down to 20 m. It is characterized by a porous or earthy texture and massive structure. The dominant ore minerals are hematite and limonite (about 20%), with minor pyrite and trace chalcopyrite (Figures 3f and 4d). Hematite occurs as euhedral to subhedral grains 0.1–2 mm in size, partly altered to limonite, which appears as a gel-like material mixed with hematite.

The mixed ore occupies the transitional zone between 20 m and 35 m depth, where both oxidized and primary sulfide phases coexist. Its texture and structure are intermediate between those of the oxidized and sulfide ores.

The sulfide ore occurs below 35 m. It has a granoblastic to lepidogranoblastic texture and massive to schistose structure. Pyrite becomes the main ore mineral (~8%), accompanied by a small amount of arsenopyrite (~2%). Pyrite is isotropic and forms euhedral to subhedral grains 0.01–0.6 mm across, unevenly distributed as fine veinlets or small clots (Figure 3b). Arsenopyrite is bright white with a slight cream tint, shows weak pleochroism and strong anisotropy, and occurs as rhombic, columnar, or spear-shaped euhedral crystals 0.02–1.2 mm in size, locally clustered.

Near the surface, the gangue minerals are mainly quartz (~79%) and sericite (~1%), whereas at depth, the white mica coarsens to muscovite (25%–30%), accompanied by quartz (55%–70%), minor feldspar (~5%) and carbonate bands (Figure 3c,d). Quartz is anhedral granular, displays undulatory extinction, and has serrate grain boundaries with a weakly elongated, slightly oriented fabric. Muscovite occurs as fine flakes that are aligned. Feldspar is anhedral tabular granular, turbid from alteration, and distributed as irregular aggregates.

Overall, the Caijiagou gold deposit exhibits a limited range of alteration types, mainly pyritization, silicification, sericitization, and carbonatization, indicating a low-temperature hydrothermal alteration assemblage. Products of the early stage are commonly cut and overprinted by those of later stages, resulting in the coexistence of minerals formed at different stages.

The samples analyzed in this study were collected from the No. I ore body, including deep primary sulfide ores and surface oxidized ores. Based on field observations and laboratory identification, three mineralization stages were recognized: (I) the quartz–sericite–pyrite stage, (II) the quartz–polymetallic sulfide–ankerite stage, and (III) the calcite stage. Stage II is the major mineralization stage (Figures 3b–e and 4a–c). Stage I and Stage II mineralization are mainly developed in the primary sulfide ore zone (>35 m depth), whereas the oxidized and mixed ores represent supergene modification of these primary mineralization stages. Stage III calcite veins are barren and cut across all previous mineralization.

Pyrite is the dominant ore mineral, occurring mainly in the quartz–sericite–pyrite stage (I) and the quartz–polymetallic sulfide stage (II). It is typically in euhedral to subhedral cubes (Figures 3 and 4). The distribution of pyrite in the ore is uneven. In the quartz–sericite–pyrite stage, pyrite (Py1) is fine-grained (0.05–0.2 mm) and occurs as fine disseminations in quartz and sericite (Figure 4a,b). In the quartz–polymetallic sulfide–ankerite stage, pyrite (Py2) is euhedral to subhedral granular, with larger crystal sizes (0.3–1 mm). It occurs as bands or disseminations at the margins of quartz veins and is intergrown with ankerite (Figure 4a–c). Arsenopyrite typically occurs as subhedral to euhedral grains, with common cataclastic textures. In the quartz–sericite–pyrite stage, arsenopyrite (Apy1) is relatively fine, with grain sizes of about 0.05–0.1 mm. In the quartz–polymetallic sulfide–ankerite stage, arsenopyrite (Apy2) mainly occurs as disseminations in quartz veins, with grain sizes of about 0.1–0.3 mm, intergrown with ankerite (Figure 4c).

Under microscopic observation and TIMA analysis, native gold is recognized within pyrite (Py2) of the quartz–polymetallic sulfide–ankerite stage. Apatite and sericite are also identified in the main mineralization stage, and suitable minerals are planned for subsequent in situ dating analysis. In surface-oxidized samples, pyrite has been oxidized to limonite, with native gold grains visible at the oxidation rims of pyrite (Figure 4d).

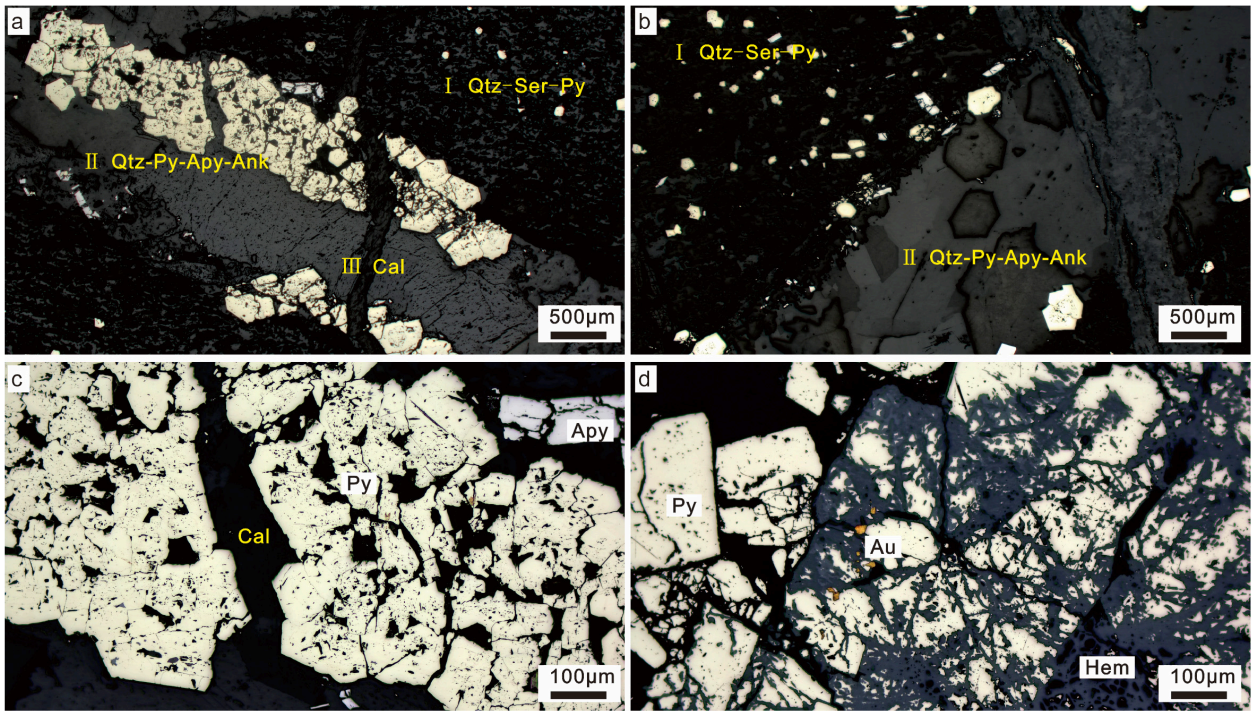


Figure 4. Photomicrograph of ore minerals. (**a**) three mineralization stages and their crosscutting relationships; (**b**) the first and second mineralization stages; (**c**) the second and third mineralization stages; (**d**) native gold at the margins of pyrite. Qtz—quartz, Ser—sericite, Py—pyrite, Apy—arsenopyrite, Ank—ankerite, Cal—calcite, Hem—hematite, Au—gold.

4. Samples and Analytical Methods

The TIMA (TESCAN Integrated Mineral Analyzer) analysis was performed to identify mineral phases and their textural relationships in the ore samples. The test was completed by Nanjing Hongchuang Geological Exploration Technology Service Co., Ltd. The instrument model used was the field emission scanning electron microscope TESCAN Mira3 LMH (TESCAN, Brno, Czech Republic), equipped with TESCAN's original BSE probe and energy-dispersive spectrometer detector (EDAX Element 30 EDAX Inc., Mahwah, NJ, USA). The voltage used by the instrument during the testing process was 25 kV, the current was 9 nA, and the working distance was 15 mm. Before TIMA testing, use a platinum Faraday cup to calibrate the BSE signal and a metal Mn to calibrate the EDS signal. The standard sample type used was MAC: 12925. During the test, dissociation mode was used to simultaneously obtain BSE images and EDS data, with an X-ray count of 1000 for each point. The BSE unit pixel size was 2.5 μm, and the energy-spectrum testing step size was 7.5 μm.

Sulfur isotopic ratios of sulfides (pyrite, pyrrhotite, arsenopyrite, chalcopyrite, sphalerite) were determined by LA-MC-ICP-MS at Nanjing Hongchuang Geological Exploration Technology Service Co. Ltd. A Resolution SE laser-ablation system (Applied Spectra, West Sacramento, CA, USA) and Neptune XT (Thermo Fisher Scientific, Braunschweig, Germany) were combined for the experiments. An MC-ICP-MS was operated at medium mass resolution with the magnet positioned off-peak on the low-mass side to monitor ^{32}S free of O-O interferences. The deep UV laser beam generated by the quasi-molecular laser was homogenized and focused onto the sulfide surface with a fluence of 4 J/cm^2. Background gases were measured for 20 s prior to 30 s of ablation using a 50 μm spot at 5 Hz. The aerosol was carried by a He gas stream to be mixed with Ar before introduction into the MC-ICP-MS. Sulfur isotope measurements were corrected for mass bias using the sample-standard bracketing method with Wenshan pyrite (δ34S = +1.5‰ V-CDT) as

the external standard. NIST SRM 123 sphalerite particles (δ34S = +17.1‰) were analyzed periodically as a secondary reference material to monitor data quality [59].

In situ trace element analyses of sulfide minerals were performed on pyrite (Py1 and Py2) and arsenopyrite (Apy1 and Apy2) from both Stage I and Stage II mineralization using LA-ICPMS at Nanjing Hongchuang Geological Exploration Technology Service Co., Ltd. The Resolution SE model laser-ablation system (Applied Spectra, West Sacramento, CA, USA) was equipped with an ATL (ATLEX 300) excimer laser and a Two-Volume S155 ablation cell. The laser ablation system was coupled to an Agilent 8900 ICPMS (Agilent, Santa Clara, CA, USA) [60]. LA-ICPMS tuning was performed using a 50-micron-diameter line scan at 3 μm/s on NIST 612 at ~3.5 J/cm^2 with a repetition rate of 10 Hz. The gas flow was adjusted to get the highest sensitivity (^{238}U~6 × 10^{5}cps) and the lowest oxide ratio (ThO/Th < 0.2%). P/A calibration was conducted on the NIST 610 using a 100-micron-diameter line scan. Other laser parameters were the same as those of the tuning: ^{23}Na, ^{25}Mg, ^{27}Al, ^{29}Si, ^{31}P, ^{39}K, ^{43}Ca,^{45}Sc, ^{47}Ti, ^{51}V, ^{52}Cr, ^{55}Mn, ^{57}Fe, ^{59}Co, ^{60}Ni, ^{66}Zn, ^{69}Ga, ^{85}Rb, ^{86}Sr, ^{89}Y, ^{90}Zr, ^{93}Nb, ^{133}Cs, ^{137}Ba, ^{139}La, ^{140}Ce, ^{141}Pr, ^{146}Nd, ^{147}Sm, ^{151}Eu, ^{157}Gd, ^{159}Tb, ^{163}Dy, ^{165}Ho, ^{166}Er, ^{169}Tm, ^{173}Yb, ^{175}Lu, ^{178}Hf, ^{181}Ta, ^{208}Pb, ^{232}Th, ^{238}U, with a total sweep time of ~0.31 s. Thin sections were fixed onto the sample holder and cleaned prior to the analysis using AR-grade methanol. Pre-ablation was conducted for each spot analysis using 5 laser shots (~1 μm in depth) to remove potential surface contamination. The analysis was performed using a 50 μm diameter spot at 5 Hz and a fluence of 4 J/cm^2. The iolite software package ('3D Trace Element', iolite v4.8.2) was used for data reduction [61,62]. Reference materials were bracketed among multiple groups of 10 to 12 sample unknowns. Typically, 40 s of sample signals was acquired after a 20 s gas background measurement. A total of 32 LA-ICP-MS spot analyses were performed on two types of pyrite and arsenopyrite from the Caijiagou deposit, including 14 analyses of Py1, 7 analyses of Py2, 4 analyses of Apy1, and 7 analyses of Apy2. The results are presented in Table 1.

Apatite U-Pb dating was conducted using LA-ICPMS at Nanjing Hongchuang Geological Exploration Technology Service Co. The Resolution SE model laser-ablation system (Applied Spectra, West Sacramento, CA, USA) was equipped with an ATL (ATLEX 300) excimer laser and a Two-Volume S155 ablation cell. The laser-ablation system was coupled to an Agilent 8900 ICPMS (Agilent, Santa Clara, CA, USA) [60]. LA-ICPMS tuning was performed using a 50-micron-diameter line scan at 3 μm/s on NIST 612 at ~3.5 J/cm^2 with a repetition rate of 10 Hz. The gas flow was adjusted to get the highest sensitivity (^{238}U~6 × 10^5 cps) and the lowest oxide ratio (ThO/Th < 0.2%). P/A calibration was conducted on NIST 610 using a 100-micron-diameter line scan. Other laser parameters were the same as those of the tuning. ^{31}P, ^{43}Ca, ^{45}Sc, ^{49}Ti, ^{86}Sr, ^{89}Y, ^{90}Zr, ^{93}Nb, ^{139}La, ^{140}Ce, ^{141}Pr, ^{146}Nd, ^{147}Sm, ^{151}Eu, ^{157}Gd, ^{159}Tb, ^{163}Dy, ^{165}Ho, ^{166}Er, ^{169}Tm, ^{173}Yb, ^{175}Lu, ^{178}Hf, ^{181}Ta, ^{202}Hg, ^{204}Pb, ^{206}Pb, ^{207}Pb, ^{208}Pb, ^{232}Th, and ^{238}U were mass-analyzed with a total sweep time of ~0.26 s. Apatite was mounted in epoxy discs, polished to expose the grains, cleaned ultrasonically in ultrapure water, then cleaned again prior to the analysis using AR-grade methanol. Pre-ablation was conducted for each spot analysis using 5 laser shots (~0.3 μm in depth) to remove potential surface contamination. The analysis was performed using a 30 μm diameter spot at 5 Hz with a fluence of 2 J/cm^2. The iolite software package was used for data reduction [61]. Madagascar and Durango apatite were used as primary and secondary reference materials, respectively [63,64]. Triplets of Madagascar and Durango were bracketed among multiple groups of 10 to 12 sample unknowns. Typically, 35–40 s of sample signals were acquired after a 20 s gas background measurement. Using the exponential function to calibrate the downhole fractionation [62]. NIST 610 and ^{43}Ca were used to calibrate the trace element concentrations as the external reference material and internal standard element, respectively.

Table 1. Trace elements (ppm) of pyrite (Py1, n = 14; for Py2, n = 7) and arsenopyrite (Apy1, n = 4; Apy2, n = 7) from Stage I and Stage II mineralization in the Caijiagou gold deposit.

	As	Sb	Ni	Co	Cu	Mn	Cr	Pb	Zn	Se	Ag	Tl	Au	V	Mo	Cd	Bi
Py1	14,772.77	6.45	130.69	31.24	12.07	5.12	2.39	101.65	0.55	23.19	2.33	0.01	1.84	0.44	-	0.01	1.56
	12,303.98	4.99	102.50	46.03	8.65	499.99	6.45	58.88	4.86	19.46	3.51	0.17	0.79	10.42	0.02	-	0.96
	15,568.04	5.42	119.57	18.79	20.77	-	5.54	37.51	0.87	-	1.39	0.00	1.52	7.70	0.45	-	0.72
	16,377.88	10.12	276.82	27.17	56.98	0.91	6.93	95.86	1.59	-	2.71	-	1.72	2.21	-	-	1.59
	16,177.76	18.07	691.99	71.46	77.30	0.70	6.60	241.28	1.79	16.48	27.10	0.09	22.50	1.99	-	0.18	2.63
	16,078.50	14.21	139.61	24.27	23.84	0.80	1.35	338.41	0.93	11.84	4.38	0.03	5.57	0.75	-	0.09	1.36
	14,726.28	14.70	699.54	126.99	40.23	3.53	12.87	2444.63	4.40	26.76	16.34	0.11	2.93	6.35	-	0.16	19.27
	10,218.63	150.42	7.67	5.59	182.28	2.07	10.85	1183.94	29.28	-	52.45	-	5.58	0.31	-	0.44	44.82
	7892.39	2.81	100.03	189.82	77.14	2.92	19.24	199.79	5.59	-	7.10	-	0.55	0.26	0.45	0.05	57.49
	9112.80	37.06	8.64	3.91	120.52	0.70	4.18	1106.26	13.30	-	24.46	0.01	2.45	0.05	0.04	0.28	65.35
	2386.70	45.44	12.54	19.46	73.76	-	1.34	2567.94	3.44	-	45.61	0.01	9.67	-	0.29	0.22	51.54
	9725.58	0.83	23.37	46.24	84.80	-	-	17.98	0.37	-	2.79	-	0.39	-	0.04	0.03	22.71
	1006.55	7.23	33.83	109.34	104.25	-	2.86	428.06	4.52	-	25.43	0.03	1.58	-	-	0.08	165.65
	3422.96	171.91	42.02	109.66	278.35	-	3.21	780.26	13.42	19.96	27.25	0.01	2.15	-	6.43	0.79	305.27
Py2	13,497.81	1.06	36.40	20.47	2.85	3.40	4.31	7.00	3.05	17.24	0.19	0.02	1.10	3.02	-	-	0.17
	10,415.12	6.24	705.46	200.12	13.13	9.00	8.76	58.67	5.35	18.95	2.32	0.12	2.73	10.73	0.07	-	2.07
	13,755.73	6.12	96.98	27.46	14.23	25.57	16.59	110.89	14.74	29.14	4.49	0.04	1.34	3.44	-	0.04	5.80
	15,241.01	8.14	139.31	19.60	19.15	560.92	31.62	208.08	14.07	20.09	4.59	0.06	7.46	7.51	0.14	0.05	5.77
	17,522.90	7.39	38.79	2.75	17.17	2.70	2.91	172.56	2.03	-	4.59	0.03	3.58	1.13	-	0.06	2.34
	2602.39	7.03	31.60	13.23	13.38	2377.53	0.85	70.12	9.08	18.75	2.57	0.03	0.32	0.94	0.05	0.13	0.76
	12,567.32	10.01	117.74	28.29	32.06	2.45	2.38	137.78	1.60	-	3.78	0.02	3.50	0.74	-	0.05	1.39

Table 1. *Cont.*

	As	Sb	Ni	Co	Cu	Mn	Cr	Pb	Zn	Se	Ag	Tl	Au	V	Mo	Cd	Bi
Apy1	244,540.30	313.56	128.56	34.15	3.48	1.36	12.15	21.46	2.18	0.00	1.01	0.03	1.81	15.98	0.38	0.03	0.63
	228,338.13	376.20	14.68	3.86	2.93	16.81	7.54	9.33	1.93	0.00	0.79	0.03	0.31	15.40	1.24	0.02	0.84
	241,833.62	295.25	10.24	1.62	0.96	0.98	1.85	2.30	0.41	0.06	0.24	0.01	0.22	1.90	1.98	0.01	0.33
	239,951.13	405.41	101.52	54.75	2.08	0.30	1.71	18.93	0.48	0.23	0.59	0.01	0.68	0.79	4.54	0.03	1.41
Apy2	248,764.01	308.00	99.51	14.57	7.31	66.06	0.69	510.95	2.02	0.30	5.63	0.03	1.00	0.26	1.34	0.04	4.35
	248,023.89	212.13	15.25	4.12	1.52	0.12	0.78	14.67	0.33	0.01	0.93	0.00	0.87	0.04	0.86	0.00	0.54
	257,318.05	172.80	31.84	7.47	4.61	1.93	0.55	99.34	0.35	0.45	3.30	0.03	4.06	0.13	0.20	0.04	1.27
	258,372.15	240.07	176.15	43.80	3.91	0.13	0.60	51.58	0.46	0.28	0.99	0.00	1.79	0.00	0.06	0.02	0.88
	250,945.45	194.99	370.00	75.51	2.63	0.44	4.89	13.17	0.81	0.34	1.16	0.03	2.34	1.10	1.13	0.04	0.57
	253,761.62	204.96	14.59	2.40	3.82	0.97	1.43	16.87	0.61	0.51	1.32	0.01	0.55	0.32	1.05	0.03	0.58
	252,106.74	114.91	406.92	68.65	5.55	0.36	1.15	20.14	0.97	0.17	1.45	0.05	3.04	0.75	0.56	0.01	0.96

5. Analytical Results

5.1. Trace Element Composition of Pyrite and Arsenopyrite

The main trace elements in pyrite include As, Cu, Pb, Zn, Ag, Au, and other trace elements. Pyrite in the mining area generally has high As contents. Early-formed pyrite tends to have similar or higher trace element contents than late-formed pyrite (Figure 5).

Gold concentrations in Py1 range from 0.39 to 22.5 ppm (average ~4.0 ppm). Among the elements analyzed, Ag, Pb, Cu, Zn, Sb and Co show moderate concentrations with highly variable ranges: Ag 2.3–52.4 ppm (average ~17.0 ppm), Pb 18.0–2567 ppm (average ~637 ppm), Cu 8.6–278 ppm (average ~87 ppm), Zn 0.37–29.3 ppm (average ~6.8 ppm), Sb 0.83–172 ppm (average ~35.3 ppm), and Co 3.9–190 ppm (average ~69 ppm). Of the two pyrite types, Py1 has the highest As concentrations (1006–16,377 ppm, average ~10,697 ppm), along with elevated Ni (7.7–700 ppm) and Bi (0.03–166 ppm) (Table 1, Figure 5).

Gold concentrations in Py2 range from 0.32 to 7.46 ppm (average ~2.86 ppm). Compared with Py1, most trace elements in Py2 (e.g., Au, Cu, Pb, Ag, Sb) are markedly depleted. However, Py2 contains very high Mn (2.4–2378 ppm, average ~425 ppm) and Se (17–29 ppm, average ~21 ppm), together with moderate As (2602–17,522 ppm, average ~12,229 ppm), Ni (31.6–705 ppm, average ~166 ppm), Co (2.8–200 ppm, average ~44 ppm) and Cu (2.85–32.06 ppm, average ~15 ppm). Overall, from the early stage (Py1) to the late stage (Py2), Au, As, Pb, Zn and Ag in pyrite decrease, whereas Mn and Se become relatively enriched (Table 1, Figure 5).

Gold concentrations in Apy1 range from 0.22 to 1.82 ppm (average ~0.76 ppm). Apy1 has extremely high As (22.8–24.4 wt%, average ~23.8 wt%), together with moderate Sb (295–406 ppm, average ~348 ppm), Ni (10–129 ppm, average ~64 ppm), Co (1.6–54.8 ppm, average ~23.6 ppm) and Bi (0.33–1.41 ppm, average ~0.8 ppm). Of the two arsenopyrite types, Apy1 shows relatively low Cu (0.96–3.48 ppm, average ~2.4 ppm), Zn (0.41–2.18 ppm, average ~1.3 ppm) and Pb (Pb 2.30–21.5 ppm, average ~13 ppm) (Table 1, Figure 5).

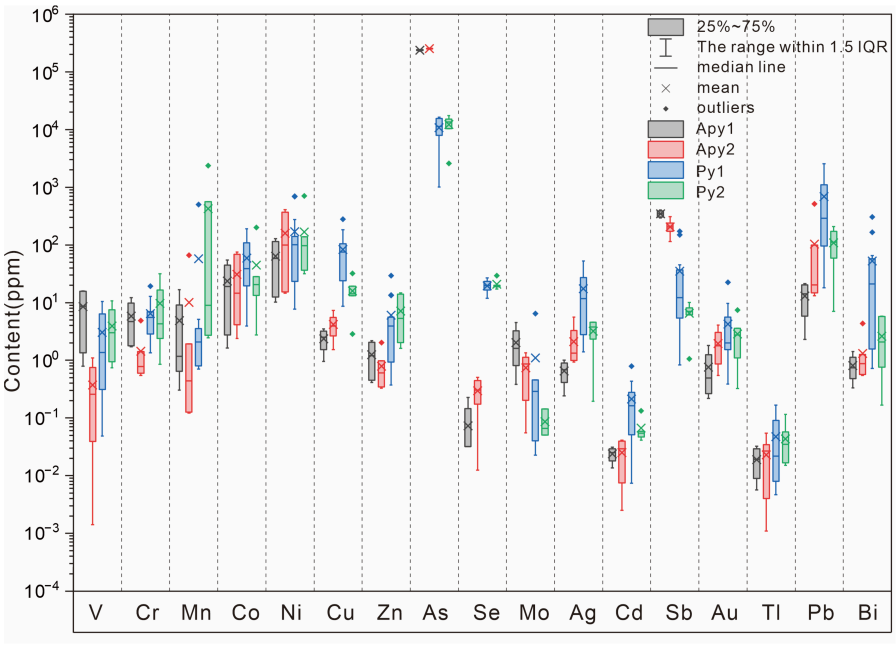


Figure 5. Comparison of trace element content characteristics of pyrite from Py1, Py2, Apy1, and Apy2 in the Caijiagou gold deposit.

Gold concentrations in Apy2 range from 0.55 to 4.06 ppm (average ~1.95 ppm). Apy2 also has very high As (24.8–25.8 wt%, average ~25.4 wt%), but relative to Apy1, it is

significantly enriched in Pb (13.2–511 ppm, average ~110 ppm), Ag (0.93–5.63 ppm, average ~2.0 ppm), Cu (1.52–7.31 ppm, average ~4.2 ppm) and Bi (0.54–4.35 ppm, average ~1.3 ppm), whereas Ni and Co show large variations (Ni 14.6–407 ppm, average ~129 ppm; Co 2.4–75.5 ppm, average ~30.9 ppm). In addition, Mn contents in Apy2 are generally higher than in Apy1 (average ~10 ppm in Apy2 vs. ~5 ppm in Apy1). From the early stage (Apy1) to the late stage (Apy2), ore-related elements such as Au, Pb, Ag, Cu and Bi are markedly enriched in arsenopyrite. This trend is opposite to that observed in pyrite, implying that different sulfide minerals have distinct controls on trace element incorporation (Table 1, Figure 5).

5.2. In Situ Sulfur Isotope Analysis of Pyrite

Table 2 presents the results of sulfur isotopic ratios of sulfides obtained by laser ablation–inductively coupled plasma mass spectrometry (LA-MC-ICP-MS).

The $\delta^{34}S$ values of 21 pyrite samples from the Caijiagou gold deposit are all positive, ranging from 6.47‰ to 10.62‰ (V-CDT), with a mean of 8.27‰. The data are relatively clustered, and the sulfur isotope compositions from the early to late stages are broadly consistent. For the Stage I mineralization (quartz–sericite–pyrite stage), $\delta^{34}S$ values range from 6.47‰ to 10.62‰, with an average of 8.12‰. For the Stage II mineralization (quartz–polymetallic sulfide–ankerite stage), $\delta^{34}S$ values range from 7.65‰ to 9.23‰, averaging 8.56‰ (Table 2).

Table 2. Sulfur isotopic compositions of pyrite (Py1, *n* = 14; Py2, *n* = 7) and arsenopyrite (Apy1, *n* = 4; Apy2, *n* = 7) from Stage I and Stage II mineralization in the Caijiagou gold deposit.

Sample No.	Minerals	$\delta^{34}S_{VCDT}$, (‰)
74Py1-1	Pyrite	8.66
74Py1-2		9.60
74Py1-3		7.73
74Py1-4		8.48
74Py1-5		10.62
74Py1-6		8.10
74Py1-7		9.36
100Py1-1		6.47
100Py1-2		7.65
100Py1-3		8.17
100Py1-4		8.01
100Py1-5		7.18
100Py1-6		6.85
100Py1-7		6.87
74Py2-1		8.70
74Py2-2		9.23
74Py2-3		8.12
74Py2-4		7.65
74Py2-5		8.65
74Py2-6		9.05
74Py2-7		8.52

Table 2. *Cont.*

Sample No.	Minerals	$\delta^{34}S_{VCDT}$, (‰)
74Apy1-1	Arsenopyrite	10.34
74Apy1-2		10.29
74Apy1-3		11.96
74Apy1-4		11.30
74Apy2-1		6.71
74Apy2-2		9.33
74Apy2-3		9.01
74Apy2-4		9.93
74Apy2-5		8.58
74Apy2-6		8.24
74Apy2-7		9.39

The $\delta^{34}S$ values of 11 arsenopyrite samples from the Caijiagou gold deposit are all positive, ranging from 6.71‰ to 11.96‰ (V-CDT) with an average of 8.56‰. The $\delta^{34}S$ values show a clear decreasing trend from the early to the late stage. For the Stage I mineralization (quartz–sericite–pyrite stage), the $\delta^{34}S$ values range from 10.34‰ to 11.96‰, averaging 10.97‰. For the Stage II mineralization (quartz–polymetallic sulfide–ankerite stage), the $\delta^{34}S$ values range from 6.71‰ to 9.93‰, averaging 8.74‰ (Table 2).

5.3. In Situ Apatite U-Pb Dating

A total of 29 apatite grains were selected for U-Pb dating from the gold-bearing quartz–polymetallic sulfide–ankerite stage (Table 3). Because of high common Pb content in the samples, the data define a discordant array in a Tera–Wasserburg concordia diagram, yielding a lower intercept age of about 237 Ma (MSWD = 0.89) (Figure 6). This age is interpreted as the crystallization age of apatite and thus represents the timing of the main ore-forming event. The results are internally consistent within uncertainty, supporting that the Caijiagou gold deposit formed during the Indosinian orogeny.

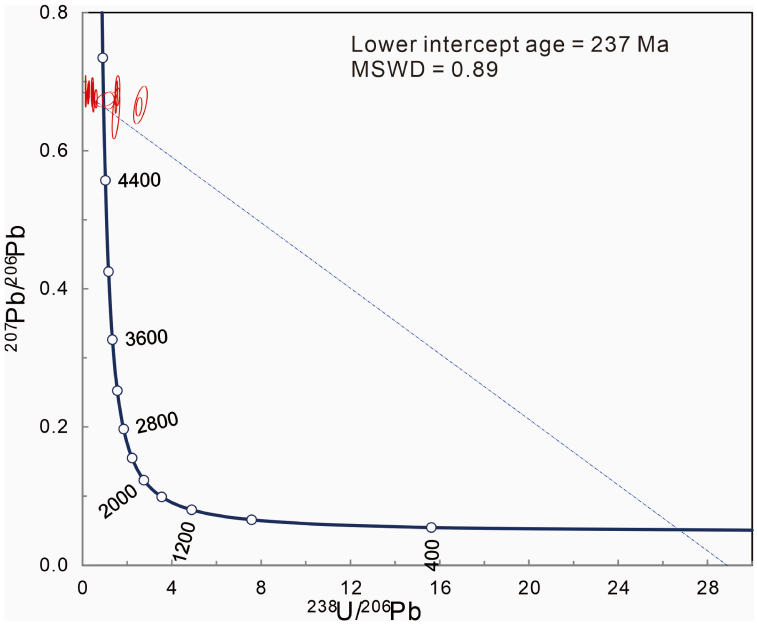


Figure 6. Concordia diagram of apatite U-Pb ages.

Table 3. U–Pb isotopic data for apatite from the main ore-stage (Stage II) of the Caijiagou gold deposit.

Samp No.	Contents/ppm					Isotope Ratio							Age/Ma					
	Sample	Total Pb	^{232}Th	^{238}U	Th/U	^{207}Pb/^{235}U	2σ	^{206}Pb/^{238}U	2σ	rho	^{207}Pb/^{206}Pb	2σ	^{207}Pb/^{235}U	2σ	^{206}Pb/^{238}U	2σ	^{207}Pb/^{206}Pb	2σ
DZ-74-1	apatite	49.09	89.43	3.92	22.84	341.77	19.07	3.72	0.22	0.97	0.68	0.01	5920	57	9926	278	4676	24
DZ-74-3	apatite	40.01	418.33	3.85	108.65	163.66	12.75	1.83	0.15	0.87	0.65	0.03	5168	74	6650	341	4624	65
DZ-74-4	apatite	31.23	38.16	8.03	4.75	105.11	4.27	1.14	0.05	0.93	0.66	0.01	4723	38	4875	132	4654	26
DZ-74-5	apatite	136.07	275.16	32.97	8.35	572.34	16.53	6.04	1.75	1.00	0.67	0.01	5964	351	10,642	1700	4675	19
DZ-74-6	apatite	30.08	171.31	2.89	59.32	341.90	35.31	3.65	0.38	0.99	0.67	0.01	5708	136	9186	586	4668	22
DZ-74-7	apatite	16.45	49.07	1.05	46.77	398.95	21.52	4.36	0.27	0.99	0.67	0.01	6059	53	10,641	259	4653	25
DZ-74-8	apatite	31.08	82.43	2.03	40.64	434.27	30.66	4.54	0.30	0.93	0.69	0.02	6158	75	11,117	296	4697	34
DZ-74-9	apatite	39.58	42.22	1.92	21.95	585.51	23.14	6.10	0.20	0.91	0.68	0.01	6461	40	12,603	186	4696	23
DZ-74-10	apatite	17.09	59.80	2.83	21.10	169.61	8.53	1.77	0.08	0.85	0.69	0.02	5196	50	6516	190	4688	38
DZ-74-11	apatite	46.65	266.47	2.10	126.74	586.25	22.16	6.16	0.23	0.93	0.68	0.01	6463	37	12,638	205	4686	23
DZ-74-12	apatite	16.03	162.87	2.48	65.65	165.59	4.26	1.75	0.04	0.42	0.68	0.02	5188	26	6514	104	4655	37
DZ-74-18	apatite	39.92	54.87	15.91	3.45	105.03	7.63	1.14	0.10	0.93	0.67	0.02	4721	75	4852	299	4654	48
DZ-74-22	apatite	72.98	38.01	3.02	12.58	634.59	28.01	6.68	0.30	0.97	0.68	0.01	6522	48	12,986	270	4696	16
DZ-74-25	apatite	57.18	42.96	2.17	19.76	738.63	38.81	7.87	0.43	0.96	0.67	0.01	6695	55	14,007	326	4683	20
DZ-74-26	apatite	15.37	2.00	0.54	3.68	790.87	36.42	8.32	0.35	0.90	0.69	0.01	6752	47	14,258	242	4694	29
DZ-74-28	apatite	30.52	6.41	1.94	3.30	432.25	19.39	4.67	0.23	0.88	0.68	0.02	6143	43	11,038	253	4668	28
DZ-74-29	apatite	33.22	7.08	1.59	4.46	574.32	25.91	6.08	0.28	0.94	0.69	0.01	6428	47	12,500	259	4696	24

6. Discussion

6.1. Source of the Ore-Forming Fluid

The origin of the ore-forming fluid is fundamental to understanding the genesis of the Caijiagou gold deposit. Multiple independent geochemical tracers—including sulfur isotopes, trace element compositions and Co/Ni ratios of pyrite and arsenopyrite—provide robust constraints on fluid provenance.

The $\delta^{34}S$ values of all analyzed pyrite and arsenopyrite from both early and late stages range from +6.47‰ to +11.96‰, with a narrow cluster around +8.7‰ (Table 2). These values are significantly higher than those of typical mantle or magmatic sulfur ($\delta^{34}S \approx 0$‰) and do not constitute the strongly negative values that would characterize bacterial sulfate reduction [30,38,65,66]. Instead, this range is consistent with sulfur generated by thermochemical sulfate reduction (TSR) of marine or evaporitic sulfate in sedimentary sequences at elevated temperatures (>100–150 °C) [67]. Similar $\delta^{34}S$ values (+5‰ to +15‰) are widely reported from sediment-hosted orogenic gold deposits worldwide, including the Sukhoi Log deposit in Russia [68] and the Betze-Post deposit in Nevada [69], both of which are hosted in sedimentary sequences, although their specific genetic models differ from the orogenic type proposed here. The similarity in sulfur isotope signatures across these systems suggests comparable sulfur source mechanisms (thermochemical reduction of marine sulfate) operating in different tectonic settings. Recent studies in the WQO have documented comparable $\delta^{34}S$ ranges for orogenic gold systems, such as the Liba gold deposit ($\delta^{34}S$ = +5.9‰ to +12.4‰) [20,22,26] and the Baguamiao gold deposit ($\delta^{34}S$ = +6.2‰ to +11.3‰) [4,38]. These values are highly similar to those of the sulfur isotopic compositions of sulfides from Indosinian gold deposits hosted in Devonian and Carboniferous strata in the WQO (Figure 7), reinforcing the regional applicability of this signature [35,47,48]. The $\delta^{34}S$ values of pyrite (Py2) and arsenopyrite (Apy2) in the quartz–polymetallic sulfide–ankerite stage are lower than those in Stage I. This decrease may be attributed to the influx of cooler, oxidized meteoric water during the late stage of mineralization, which altered the physicochemical conditions (e.g., temperature, oxygen fugacity, and pH) of the ore fluid and thus affected sulfur isotope partitioning. Alternatively, the shift could reflect mixing with a fluid component that had undergone sulfate reduction in a more open system or that was derived from isotopically lighter sedimentary sulfides. However, regardless of the exact mechanism, the overall $\delta^{34}S$ range remains consistently positive and falls within the field characteristic of crustal sulfur sources (Figure 7).

The Co/Ni ratios of pyrite and arsenopyrite provide additional discrimination. It has long been established that magmatic–hydrothermal pyrite typically exhibits Co/Ni > 1, whereas sedimentary/diagenetic pyrite has Co/Ni < 1 [9,12,14,34,70,71]. In the present deposit, the late-stage, gold-bearing pyrite (Py2) shows Co/Ni ratios uniformly below 1, ranging from 0.07 to 0.56 (average 0.28), and both generations of arsenopyrite (Apy1 and Apy2) also yield Co/Ni ratios < 1. The early pyrite (Py1) displays a wider range, with most values < 1 but five grains exceeding 1 (1.9–3.2, average 2.25) (Figure 8). This scatter is interpreted as reflecting local kinetic effects, micro-scale heterogeneity, or incorporation of relict diagenetic pyrite in the early fluid pathway, rather than indicating a separate high-Co fluid pulse. Crucially, arsenopyrite—which forms under low sulfur fugacity—never records Co/Ni > 1, confirming that the main ore-forming fluid was persistently depleted in Co relative to Ni. Such a signature is characteristic of metamorphic or sedimentary basinal fluids that have extensively interacted with Ni-rich crustal rocks [72,73]. A global compilation of trace element data from 67 orogenic gold deposits indicates that Co/Ni ratios in these systems typically fall within the range of 0.2–1.5 [72], consistent with the observations here.

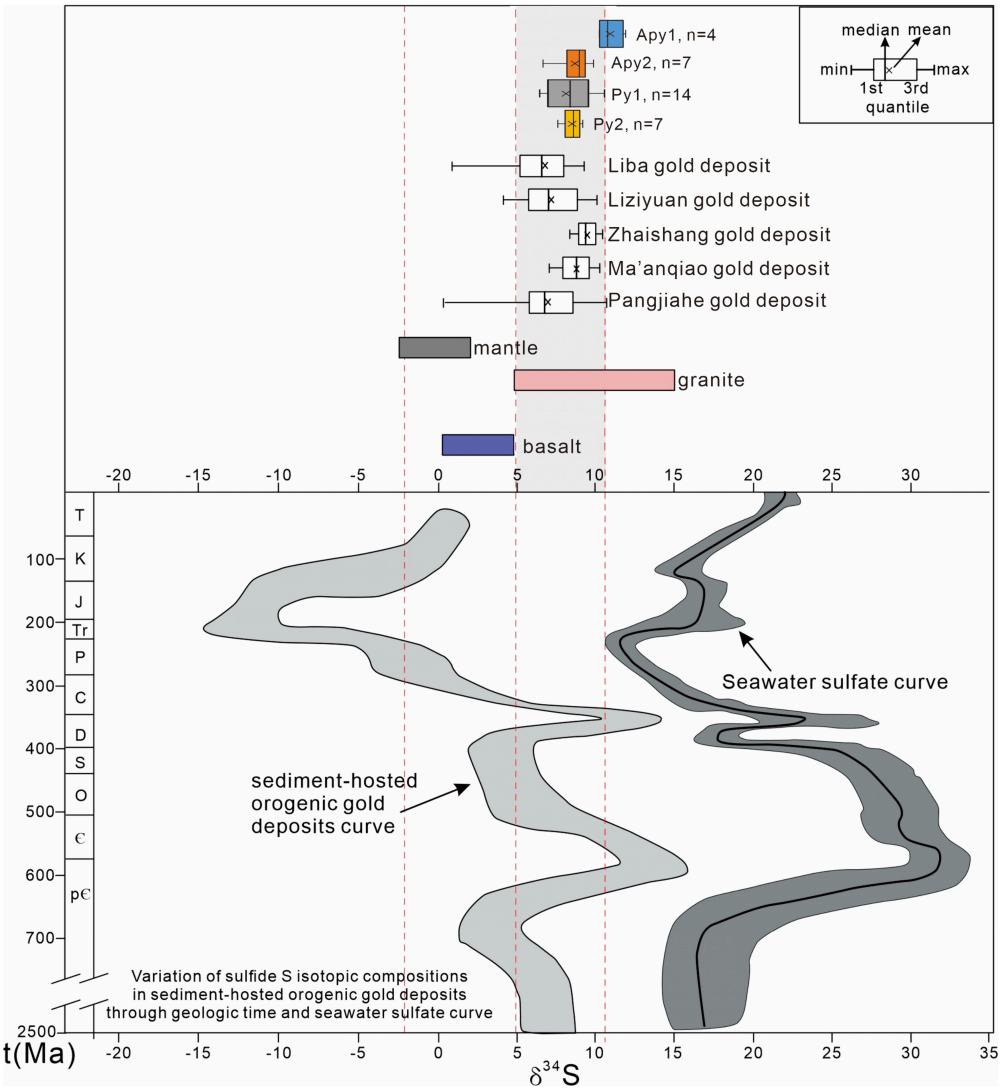


Figure 7. S-isotope distribution map of sulfide from ores of the Caijiagou and neighboring gold deposits.

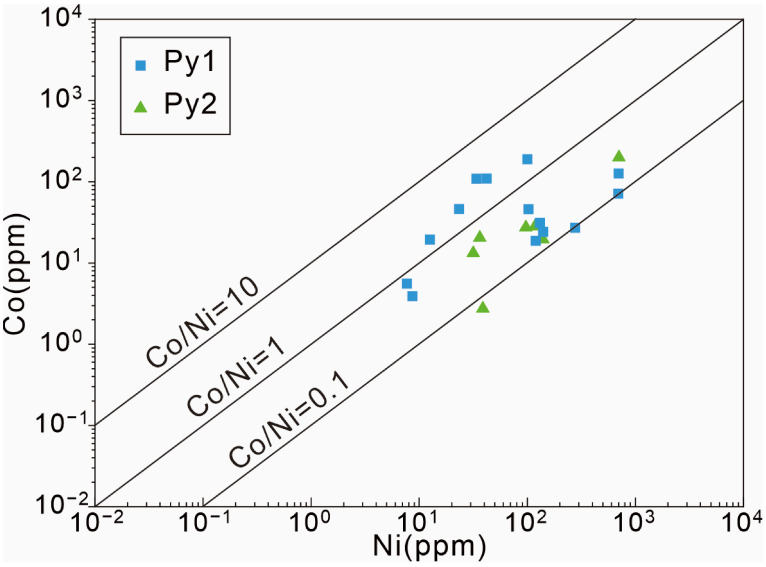


Figure 8. Co/Ni ratio scatter plot of pyrite from ores of the Caijiagou and neighboring gold deposits.

Trace element geochemistry further characterizes the fluid and gold enrichment processes. Both generations of arsenopyrite contain extremely high As contents, typically exceeding 240,000 ppm, with As/Ni ratios on the order of 10^3–10^4, reflecting strong As–Ni decoupling under low sulfur fugacity [74,75]. Gold concentrations in arsenopyrite reach several ppm, with Au/As ratios of ~10^{-5} to 10^{-4}, comparable to values reported for gold deposited from reduced, low-salinity bisulfide complexes [76,77]. The low Ag/Au ratios in late pyrite and arsenopyrite (mostly <10) indicate that gold precipitated as native metal rather than electrum, consistent with deposition from a reduced, CO_2-rich fluid where gold-bisulfide complexes were destabilized by sulfidation or cooling [78,79]. The presence of ankerite as a vein mineral throughout the main ore stage further supports a CO_2-rich, reduced fluid composition, as ankerite is a diagnostic gangue in orogenic gold systems worldwide [80,81].

Collectively, the $\delta^{34}S$ values, Co/Ni ratios and trace element signatures converge on a single, coherent conclusion: the ore-forming fluid was a crustal, moderately reduced, CO_2-bearing fluid with no significant contribution from magmatic or mantle sources. The minor Co/Ni > 1 signature in early Py1 may record a transient pulse of magmatic fluid, but the overwhelming evidence points to a dominantly metamorphic or sedimentary basinal fluid for the main gold event.

6.2. Timing of Mineralization

The timing of mineralization is critical for placing the Caijiagou deposit in its regional tectonic context and for understanding its genetic relationship with surrounding magmatic and metamorphic events. Apatite from the gold-bearing quartz–polymetallic sulfide–ankerite stage (main ore stage) was selected for in situ U Pb dating. Twenty-nine apatite grains were analyzed, and despite high common Pb contents, the data define a well-constrained discordia on the Tera–Wasserburg concordia diagram, yielding a lower intercept age of 237 Ma (MSWD = 0.89) (Figure 6). This age is interpreted as the crystallization age of apatite and thus represents the timing of the main gold mineralization event.

This Middle Triassic age coincides precisely with the Indosinian orogeny, the collisional event between the North China and South China Blocks [9,31,43,44,81,82]. During this period, large-scale crustal thickening and subsequent exhumation generated voluminous metamorphic fluids through prograde devolatilization of carbonaceous and pyritic sedimentary sequences—exactly the fluid type identified from the isotopic and trace element data. Numerous gold deposits in the WQO have been dated to the Triassic, with ages clustering between 240 and 220 Ma [2–4,16,27,32,38,46,83,84]. For example, rutile U-Pb dating of the Liba gold deposit in West Qinling gave an age ranging from 235 to 228 Ma [84], and the Huayagou gold deposit yielded a Late Triassic age of ca. 225 Ma [17]. The Dashui gold deposit has been dated to the Late Triassic to Early Cretaceous [85]. The 237 Ma age obtained here is therefore fully consistent with a metamorphic–devolatilization model during the Indosinian orogeny.

Importantly, there is no known Triassic magmatism of sufficient scale in this immediate area to drive an independent magmatic–hydrothermal gold system. The regional Indosinian granitoids (e.g., Tianzishan pluton) are largely coeval with or slightly older than the mineralization [31], but the absence of direct spatial association between the ore bodies and any large intrusion, together with the crustal sulfur and lead isotopic signatures, argues against a magmatic-dominated model. Instead, the heat from these intrusions may have enhanced metamorphic fluid circulation and metal leaching from the sedimentary pile, but the fluids themselves were predominantly of metamorphic origin [2,23,24].

6.3. Integrated Ore-Forming Model

Integrating all lines of evidence—the crustal source of sulfur and metals ($\delta^{34}S$ = +6.5‰ to +12.0‰; Co/Ni ratios < 1 in main ore-stage sulfides), the Middle Triassic apatite age (237 ± 4.3 Ma), the systematic trace element evolution from early to late sulfides, and the mineral paragenesis (pyrite + arsenopyrite + ankerite + native gold)—a coherent genetic model for the Caijiagou gold deposit is proposed.

During the Middle Triassic Indosinian orogeny, collision between the North China and South China Blocks caused intense crustal thickening and regional metamorphism of the Silurian Taiyangsi Formation metasedimentary rocks (Figure 9) [4,33–35]. Prograde devolatilization of buried carbonaceous and pyritic sedimentary sequences generated large volumes of reduced, CO_2-rich metamorphic fluids (Figure 9). These fluids carried gold and inherited a $\delta^{34}S$ signature of +6.5‰ to +12.0‰ from the sedimentary pile [67,68]. The fluids also extracted Co, Ni, Pb and other metals from the same sedimentary rocks. Due to the reducing, low-fS_2 conditions, Ni was preferentially incorporated into sulfides relative to Co, resulting in the consistently low Co/Ni ratios observed in all ore-stage sulfides [72].

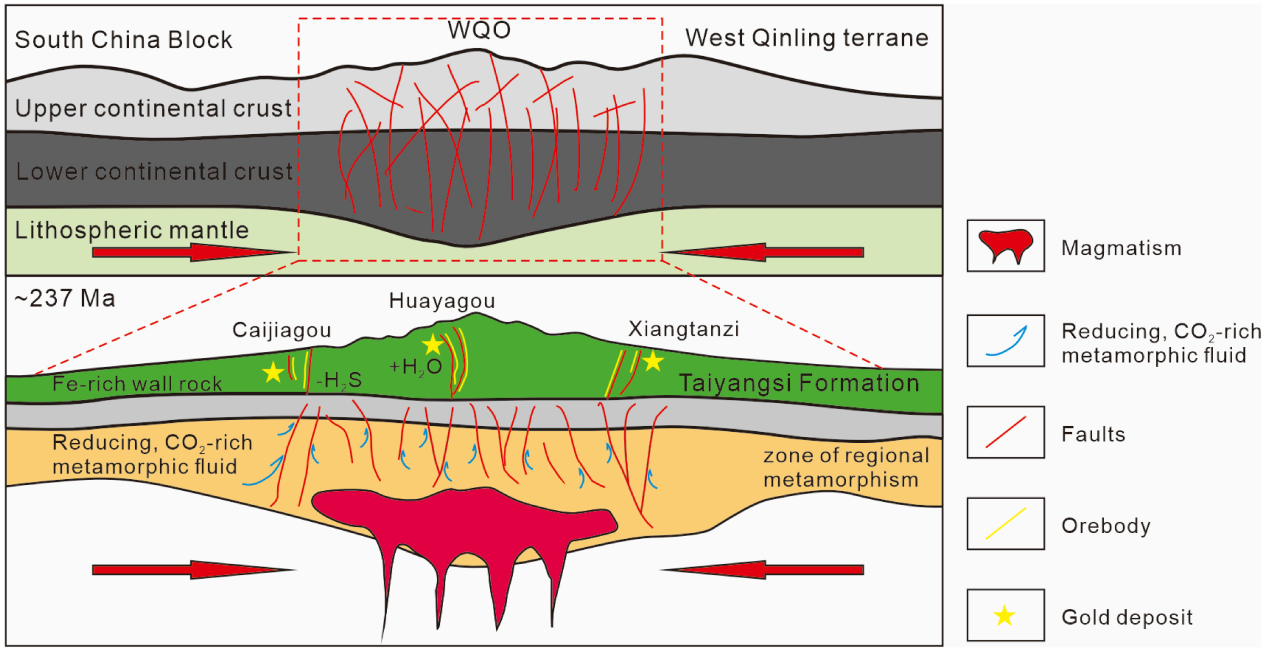


Figure 9. Metallogenic model of the Caijiagou gold deposit [17].

As the fluids ascended along crustal-scale fault zones (the F4 fault and its secondary structures), they encountered and interacted with the Taiyangsi Formation. This interaction caused sulfidation—the reaction of H_2S with ferrous iron to form pyrite and arsenopyrite (Figure 9). This process consumed H_2S, reducing the solubility of gold–bisulfide complexes and triggering rapid precipitation of native gold [78]. The gold is primarily hosted as invisible gold in pyrite and arsenopyrite, with minor native gold inclusions visible in oxidized samples at the margins of altered pyrite grains. The appearance of ankerite indicates that the fluid was also saturated with respect to carbonate, which precipitated as the CO_2 concentration decreased due to pressure release or cooling. The decreasing Co/Ni ratios from early Py1 (some >1) to late Py2 (all <0.6) record progressive cooling and reduction of the fluid. The low Ag/Au ratios throughout the main stage confirm that gold precipitated as native metal rather than electrum, consistent with an orogenic gold system [4,14,17,78].

The proposed model satisfies all the defining characteristics of orogenic gold deposits [80,81]: spatial and temporal association with an orogenic belt (Indosinian); formation from reduced metamorphic fluids; mineral assemblages including pyrite, arsenopyrite, ankerite and native gold; crustal sulfur and metal sources (non-magmatic); and formation at moderate temperatures during convergent tectonics. The Caijiagou deposit is therefore classified as a sediment-hosted orogenic gold system formed during the Indosinian collisional orogeny.

From an exploration perspective, positive $\delta^{34}S$ values (+6‰ to +12‰), low Co/Ni ratios (<0.6) in ore-stage sulfides, and Triassic apatite ages constitute diagnostic fingerprints for targeting similar deposits within the WQO. The close spatial relationship between gold mineralization and intermediate-acidic dykes observed in the Caijiagou deposit, as well as in other West Qinling gold deposits such as Liba and Huayagou [2,17,83,84], suggest that dyke swarms may serve as an indirect exploration guide, indicating areas of enhanced fluid flow and structural preparation.

7. Conclusions

The Caijiagou gold deposit in the WQO was investigated through systematic petrography, in situ trace element and sulfur isotope analyses of pyrite and arsenopyrite, and apatite U-Pb geochronology. The following conclusions are drawn.

(1) The ore-forming fluid is of crustal origin. Sulfur isotopes ($\delta^{34}S$ = +6.5‰ to +12.0‰) indicate sulfur derived from thermochemical reduction of marine sulfate within the sedimentary sequence. The consistently low Co/Ni ratios (<0.6) in main ore-stage pyrite and arsenopyrite, together with low Ag/Au ratios and the presence of ankerite, support a metamorphic or sedimentary basinal fluid source rather than a magmatic–hydrothermal origin. The early pyrite (Py1) shows mixed Co/Ni ratios, with few grains > 1, which may record a transient magmatic fluid pulse, but the overwhelming evidence points to a dominantly metamorphic fluid for the main gold event.

(2) Apatite from the main ore stage yields a U-Pb lower-intercept age of 237 ± 4.3 Ma (MSWD = 0.89), placing the gold mineralization in the Middle Triassic. This age coincides with the Indosinian orogeny, consistent with numerous other gold deposits in the West Qinling belt.

(3) During the Middle Triassic Indosinian, crustal thickening and metamorphism of the Silurian Taiyangsi Formation generated reduced metamorphic fluids. These fluids transported gold as bisulfide complexes and precipitated it when sulfidation of Fe-rich wall rocks consumed H_2S, destabilizing the gold complexes. The deposit is classified as a sediment-hosted orogenic gold system. These geochemical and geochronological features—positive $\delta^{34}S$ values, low Co/Ni ratios in ore-stage sulfides, and Triassic apatite ages—support an orogenic genesis for the Caijiagou deposit in the WQO.

Author Contributions: Conceptualization, X.S. and W.L.; methodology, W.L.; software, S.L.; validation, X.S., W.L. and C.W.; formal analysis, X.S.; investigation, X.S.; resources, X.S.; data curation, Z.L.; writing—original draft preparation, X.S.; writing—review and editing, W.L.; visualization, W.L.; supervision, J.M.; project administration, X.S.; funding acquisition, X.S. All authors have read and agreed to the published version of the manuscript.

Funding: This research was funded by the Geological Exploration Fund of Gansu Province through the project "Prospecting of Gold and Polymetallic Deposits in the Caijiagou Area, Liangdang County, Gansu Province", grant number "202301-D20"; the Geological Craftsman Fund Program of the Engineering Research Center of Mineral Resources Comprehensive Exploration, Utilization and Protection, Gansu Province, grant number "YD202408".

Data Availability Statement: The original contributions presented in this study are included in the article. Further inquiries can be directed to the corresponding author.

Acknowledgments: Many thanks are expressed to the anonymous reviewers for their constructive criticism and suggestions on an earlier draft of the manuscript.

Conflicts of Interest: Author Wei Li was employed by the Xi'an Mineral Resources Survey, China Geological Survey. The remaining authors declare that the research was conducted in the absence of any commercial or financial relationships that could be construed as a potential conflict of interest.

Abbreviations

The following abbreviations are used in this manuscript:

WQO West Qinling Orogen

References

1. Gao, Y.; Li, X.; Gu, P.; Ma, Z.; Zhuang, Y.; Guo, Z.; Zhao, X. The geodynamic setting of Triassic large-scale mineralization event in the West Qinling Orogen: Evidence from high-Mg andesite in the Qiadong Copper deposit. *Acta Petrol. Sin.* **2022**, *38*, 3143–3164. (In Chinese) [CrossRef]
2. Yang, T.; Zhu, L.; Hu, Y.; Long, D.; Wang, F.; Xia, Y.; Liu, W.; Jiang, H.; Liu, Z. Genesis of the Liba Gold Deposit in West Qinling: Evidence from Fluid Inclusions and Zircon U-Pb Dating in Gold Bearing Quartz Vein. *Northwest. Geol.* **2026**, *59*, 60–78. (In Chinese)
3. Si, M.; Liu, J.; Zhang, B.; Cao, R.; Lai, Z.; Fan, R.; Yu, Q.; Du, B. Study on Occurrence State and Genesis of Gold Mineral in the Dadiangou Gold Deposit, Gansu Province. *Gold Sci. Technol.* **2025**, *33*, 19–31. (In Chinese)
4. Mao, C.; Lü, X.; Jiang, S.; Sun, B.; Ruan, B.; Chen, C. The genesis of the baguamiao orogenic gold deposit linked to multistage ore-forming processes in triassic tectonic transition of south Qinling, China. *Ore Geol. Rev.* **2024**, *166*, 105964. [CrossRef]
5. Han, B.; Jiang, Y.; Liu, Y.; Ni, C. Middle to late triassic felsic and mafic magmatism in the eastern West Qinling orogen, central China: A record of the paleo-tethyan oceanic crust advance to retreat. *Lithos* **2024**, *464–465*, 107451. [CrossRef]
6. Qiu, K.; Deng, J. Petrogenesis of granitoids in the dewulu skarn copper deposit: Implications for the evolution of the paleotethys ocean and mineralization in Western Qinling, China. *Ore Geol. Rev.* **2017**, *90*, 1078–1098. [CrossRef]
7. Kong, Y.; Chen, G.; Liu, B.; Xie, M.; Yu, Z.; Li, C.; Wu, Y.; Gao, Y.; Zha, S.; Zhang, H.; et al. 3d mineral prospectivity mapping of zaozigou gold deposit, West Qinling, China: Machine learning-based mineral prediction. *Minerals* **2022**, *12*, 1361. [CrossRef]
8. Li, Z.; Pei, X.; Wei, L.; Liang, G.; Wang, M.; Li, R.; Pei, L.; Liu, C.; Chen, Y.; Gao, F. Detrital zircon geochronology of early triassic strata in the West Qinling orogen: Implications for the tectonic evolution of the paleo-tethyan ocean. *J. Earth Sci.* **2024**, *35*, 1087–1106. [CrossRef]
9. Yang, H.; Yang, F.; Jepson, G.; Bagas, L.; Tu, J.; Li, H.; Qian, Z. Magmatic and hydrothermal evolution of the superlarge dashui goldfield in the West Qinling orogen, China. *Ore Geol. Rev.* **2024**, *169*, 106095. [CrossRef]
10. Guo, Q.; Zhang, J.; Mao, X.; Wu, Y. Petrogenesis of Cambrian plagiogranites in the Shangdan suture zone of the West Qinling: Insights to subduction initiation of the Proro-Tethys. *Acta Petrol. Mineral.* **2024**, *43*, 304–329. (In Chinese)
11. Li, P.B. Study on the Characteristics of Ductile Shear Zone in the Pangjiahe Gold Deposit. *J. Henan Sci. Technol.* **2019**, *34*, 95–97. (In Chinese)
12. Fan, C.; Yu, H.; Tamer, M.T.; Zhang, L.; Wang, J.; Liu, P.; Xue, X.; Li, C.; Wang, Y. Ore genesis of the nanban gold deposit, West Qinling orogen: Insights from monazite geochronology and geochemistry of sulfides. *Ore Geol. Rev.* **2025**, *179*, 106531. [CrossRef]
13. Wei, K. Geological Features and Metallogenic Regularity of SuiShiZi Gold Deposit in LiZiYuan, TianShui. Master's Thesis, Chang'an University, Xi'an, China, 2011.
14. Qiu, K.; Deng, J.; Yu, H.; Rasbury, T.; Tang, Y.; Zhu, R.; Zhang, P.; Goldfarb, R. The zaozigou orogenic gold-antimony deposit, West Qinling orogen, China: Structural controls on multiple mineralization events. *Geol. Soc. Am. Bull.* **2024**, *136*, 4218–4232. [CrossRef]
15. Wang, S.; Liu, Z.; Liu, Y.; Deng, N.; Yang, B.; Tan, L. Contribution of triassic tectonomagmatic activity to the mineralization of liziyuan orogenic gold deposits, West Qinling orogenic belt, China. *Minerals* **2023**, *13*, 130. [CrossRef]
16. He, C. Geology, Mineralization, and Genesis of Typical Gold Deposits in the Northern Belt of the West Qinling Orogen. Ph.D. Thesis, China University of Geosciences, Wuhan, China, 2022.
17. Teng, F.; Yan, K.; Yang, K.; Bagas, L.; Gao, Y.; Wei, L.; Teng, Y.; Guo, H.; Tang, Y.; Li, G. Geological characteristics and geochronology of the huayagou au deposit, Western Qinling: Implication for regional ore genesis. *Ore Geol. Rev.* **2025**, *178*, 106456. [CrossRef]

18. Yu, H.; Fu, Y.; Liu, X.; Said, N.; Cao, H.; Liu, C.; Fang, W.; Liu, J.; Zou, H. The gold mineral systems of the West Qinling orogen, central China: New insight from the baguamiao gold deposit. *Ore Geol. Rev.* **2023**, *162*, 105705. [CrossRef]
19. Yang, L.; Wang, Q.F.; Zhao, S.Y.; Li, H.J.; Zhao, H.S.; Dong, C.Y.; Liu, X.F.; Deng, J. Structural controls on orogenic gold deposits. *Acta Petrol. Sin.* **2023**, *39*, 277–292. (In Chinese) [CrossRef]
20. Chen, Y.; Wang, Y.; Luo, J.; Li, D.; Wang, J.; Long, L.; Zhang, H.; Geng, J. Characteristics and genesis of gold-bearing sulfide in the Liba gold deposit, West Qinling. *Acta Pet. Sin.* **2025**, *41*, 1387–1405. (In Chinese) [CrossRef]
21. Jiang, Q.M. Origin and genesis of gold ore fluid in Zhongchuan area, Li County, Gansu Province. *Chin. J. Geol.* **2022**, *57*, 510–523. (In Chinese)
22. Ke, C.; Wang, X.; Yang, Y.; Tian, Y.; Li, J.; Nie, Z.; Lv, X.; Wang, S.; Gong, M. Petrogenesis of dykes and its relationship to gold mineralization in the Western Qinling belt: Constraints from zircon U-Pb age, geochemistry and Nd-Hf-S isotopes of Liba gold deposit. *Miner. Depos.* **2020**, *39*, 42–62. (In Chinese)
23. Jiao, Y.; Feng, J. Source of ore Forming Materials and Genesis of Zhupogou Gold Deposit in West Qinling Mountains. *Northwest. Geol.* **2024**, *57*, 219–229. (In Chinese)
24. Li, K.; Zhang, J.; Xu, J.; Li, H.; Zhang, Z.; Jia, R.; Zhang, S. Fluid inclusions and H-O-S-Pb isotopic characteristics of the Jiagantan gold deposit in Gannan, West Qinling. *Geol. Bull. China* **2023**, *42*, 941–952. (In Chinese)
25. Phillips, G.N.; Powell, R. Formation of gold deposits: Review and evaluation of the continuum model. *Earth-Sci. Rev.* **2009**, *94*, 1–21. [CrossRef]
26. Li, B.; Zhu, L.; Ding, L.; Ma, Y.; Xiong, X.; Yang, T.; Wang, F. Geology, isotope geochemistry, and ore genesis of the Liba gold deposit in the Western Qinling orogen, China. *Acta Geol. Sin.* **2021**, *95*, 427–448. (In Chinese)
27. Zhang, L.; Song, Y.; Hou, K.; Zhao, P.; Yuan, S. Genetic link between the kangjiawan gold deposit and late jurassic granitic magmatism, south China: Constraints from in situ calcite u-pb dating, sulfur isotope and trace elements of pyrite. *Ore Geol. Rev.* **2024**, *171*, 106191. [CrossRef]
28. Qiu, K.; Romer, R.L.; Long, Z.; Williams-Jones, A.E.; Yu, H.; Turner, S.; Wang, Q.; Li, S.; Zhang, J.; Duan, H.; et al. The role of an oxidized lithospheric mantle in gold mobilization. *Sci. Adv.* **2024**, *10*, eado6262. [CrossRef] [PubMed]
29. Wang, Y.; Wang, Q.; Groves, D.I.; Xue, S.; Wang, T.; Yang, L.; Deng, J. Volatile budgets and gold mobilization in metasomatized sub-continental lithospheric mantle. *Geochim. Cosmochim. Acta* **2024**, *376*, 1–13. [CrossRef]
30. Wang, X.; Wang, Z.; Zhang, W.; Ma, L.; Chen, W.; Cai, Y.; Foley, S.; Wang, C.Y.; Li, J.; Deng, J.; et al. Sulfur isotopes of lamprophyres and implications for the control of metasomatized lithospheric mantle on the giant jiaodong gold deposits, eastern China. *Geol. Soc. Am. Bull.* **2024**, *136*, 3405–3418. [CrossRef]
31. Han, B.; Jiang, Y.; Liu, Y.; Zhang, M. Petrogenesis and tectonic implications of triassic high-k calc-alkaline granitoids and mafic microgranular enclaves from the western West Qinling orogen, central China. *Lithos* **2024**, *482–483*, 107734. [CrossRef]
32. Guo, M.; Liu, J.; Zhai, D.; Weng, G.; Zhu, R. Discovery of scheelite in the zaozigou gold deposit of West Qinling orogen, northwest China and its implications for ore genesis. *China Geol.* **2024**, *7*, 586–588. [CrossRef]
33. Liu, X. Ore-Forming Fluids of the Xiangtanzi Gold Deposit, Liangdang, Gansu Province. Master's Thesis, China University of Geosciences, Beijing, China, 2018.
34. Zhang, Y. Characteristics and Genesis of the Xiangtanzi Gold Deposit in Gansu Province. Master's Thesis, China University of Geosciences, Beijing, China, 2017.
35. Ma, J.; Lv, X.; Dan, R.; Zhu, D.; Lu, F.; Yuan, B.; Yin, X. Ore Genesis of the Zuojiazhuang gold deposit in the West Qingling Orogen: Constraints from pyrite elements and multi-isotope analyses. *Earth Sci. Front.* **2019**, *26*, 146–162. (In Chinese)
36. Wei, J. Study on the Geological-Geochemical Characteristics and Origin of the Taiyangsi Gold Deposit, West Qinling, Gansu. Master's Thesis, Chang'an University, Xi'an, China, 2018.
37. Qiu, K.; Taylor, R.D.; Song, Y.; Yu, H.; Song, K.; Li, N. Geologic and geochemical insights into the formation of the taiyangshan porphyry copper–molybdenum deposit, Western Qinling orogenic belt, China. *Gondwana Res.* **2016**, *35*, 40–58. [CrossRef]
38. Xu, Y.; He, W.; An, F.; Cai, G. In situ S-Pb isotopes study of Baguamiao gold deposit, Western Qinling: Constraints on its ore-forming material sources and metallogenic process. *Miner. Depos.* **2023**, *42*, 773–790. (In Chinese)
39. Ma, J.; Lü, X.; Li, S.; Fu, J.; Mao, C.; Lu, F.; Yin, X.; Zhi, Q.; Zou, B. Pyrite zonation and source of gold in the pangjiahe orogenic gold deposit, West Qinling orogen, central China. *Ore Geol. Rev.* **2021**, *139*, 104578. [CrossRef]
40. Li, X.; Li, Y.; Dong, G.; Lv, X.; Xia, Q. Granitoid magmatism and tectonic evolution in the eastern part of the West Qinling: Constraints from geochemistry, zircon U-Pb chronology and Hf isotopic. *Acta Petrol. Sin.* **2021**, *37*, 1691–1712. (In Chinese) [CrossRef]
41. Song, Y.; Yang, L.; Yang, K.; Wang, B.; Ma, Z.; Wu, H.; Li, P.; Wang, Q. Characteristics, geochronology, and formation conditions of w mineralization and its relationship with au mineralization in the zhaishang gold deposit, West Qinling orogen, China. *Ore Geol. Rev.* **2023**, *163*, 105763. [CrossRef]

42. Yu, H.; Qiu, K.; Sai, S.; Mcintire, D.C.; Pirajno, F.; Duo, D.; Miggins, D.P.; Wang, J.; Jia, R.; Wu, M. Paleo-tethys late triassic orogenic gold mineralization recorded by the yidi'nan gold deposit, West Qinling, China. *Ore Geol. Rev.* **2020**, *116*, 103211. [CrossRef]
43. Zou, F.; Santosh, M.; Ma, C.; Wu, C.; Zheng, J.; Pan, F.; Gu, H.; Deng, L. Early triassic high-k granitoids and enclaves of the daheba pluton, West Qinling (China): Implications for relative contributions of crust and mantle. *J. Asian Earth Sci.* **2024**, *269*, 106177. [CrossRef]
44. Zhang, Z.; Zhang, Y.; Xu, L.; Wang, H. Geochronology, Geochemistry and Tectonic Significance of Late Triassic Adakite Granites in Tanchang-Zhouqu area of West Qinling. *Northwest. Geol.* **2024**, *57*, 232–247. (In Chinese)
45. Li, Y.; Peng, C.; Ran, X.; Xue, L.; Chai, S. Soil geochemical prospecting prediction method based on deep convolutional neural networks-taking Daqiao gold mine in Gansu province, China as an example. *China Geol.* **2022**, *5*, 71–83. [CrossRef]
46. Wang, Y.; Pu, W.; Li, T.; Yang, T.; Wang, J.; Li, K.; Liu, J.; Yuan, Z. The main types of magmatism gold deposits and their mineralization in Gansu Province. *Geol. Bull. China* **2024**, *43*, 869–884. (In Chinese)
47. Lu, F.; Lv, X.; Yang, S.; Xiao, Q.; Li, J.; Ren, L. Typomorphic characteristics of pyrites in the Pangjiahe gold deposit, Shaanxi Province and indication for deep ore prospecting. *Geol. China* **2023**, *50*, 277–288. (In Chinese)
48. Mou, G.; Dong, G.C.; Qu, H.L.; Liu, S.F.; Ai, Z.L.; Shi, P.L.; Cao, X.F. Ore-forming Fluid Evolution and Genesis of the Dadiangou Gold Deposit in the Western Qinling Metallogenic Belt. *Geoscience* **2021**, *35*, 1565–1575. (In Chinese)
49. Wu, Y.; Li, J.; Evans, K.; Vasconcelos, P.M.; Thiede, D.S.; Fougerouse, D.; Rempel, K. Late jurassic to early cretaceous age of the Daqiao gold deposit, West Qinling orogen, China: Implications for regional metallogeny. *Miner. Depos.* **2019**, *54*, 631–644. [CrossRef]
50. Yu, H.; Guo, C.; Qiu, K.; Mcintire, D.; Jiang, G.; Gou, Z.; Geng, J.; Pang, Y.; Zhu, R.; Li, N. Geochronological and geochemical constraints on the formation of the giant zaozigou au-sb deposit, West Qinling, China. *Minerals* **2019**, *9*, 37. [CrossRef]
51. Li, P. Characteristics and Prospecting Prediction of Brittle-ductile Shear Zone of Pangjiahe Gold Deposit in Feng County, Qinling. Master's Thesis, Chang'an University, Xi'an, China, 2020.
52. Chen, Y.; Pirajno, F.; Sui, Y. Isotope geochemistry of the tieluping silver-lead deposit, henan, China: A case study of orogenic silver-dominated deposits and related tectonic setting. *Miner. Depos.* **2004**, *39*, 560–575. [CrossRef]
53. Yang, L.; Deng, J.; Dilek, Y.; Qiu, K.; Ji, X.; Li, N.; Taylor, R.D.; Yu, J. Structure, geochronology, and petrogenesis of the late triassic puziba granitoid dikes in the mianlue suture zone, Qinling orogen, China. *Geol. Soc. Am. Bull.* **2015**, *127*, 1831–1854. [CrossRef]
54. Luo, B. Petrogenesis and geodynamic processes of the Indosinian magmatism in the West Qinling Orogenic belt, central China. Ph.D. Thesis, Chian University of Geosciences, Wuhan, China, 2013.
55. Hu, F.; Liu, S.; Ducea, M.N.; Chapman, J.B.; Wu, F.; Kusky, T. Early mesozoic magmatism and tectonic evolution of the qinling orogen: Implications for oblique continental collision. *Gondwana Res.* **2020**, *88*, 296–332. [CrossRef]
56. Xu, X.; Chen, J.; Gao, T.; Li, P.; Li, T. Granitoid magmatism and tectonic evolution in northern edge of the Western Qinling terrane. *Acta Petrol. Sin.* **2015**, *30*, 371–389. (In Chinese)
57. Bi, M.; Li, Y.; Yang, J. Geochemical character of Chaijiazhuang, Baguashan and Tianzishan granites in Western Qinling. *Gansu Geol.* **2006**, *15*, 42–46. (In Chinese)
58. Zhang, L.; Qiu, K.; Hou, Z.; Pirajno, F.; Shivute, E.; Cai, Y. Fluid-rock reactions of the triassic taiyangshan porphyry cu-mo deposit (West Qinling, China) constrained by QEMSCAN and iron isotope. *Ore Geol. Rev.* **2021**, *132*, 104068. [CrossRef]
59. Fu, J.; Hu, Z.; Zhang, W.; Yang, L.; Liu, Y.; Li, M.; Zong, K.; Gao, S.; Hu, S. In situ sulfur isotopes (δ34s and δ33s) analyses in sulfides and elemental sulfur using high sensitivity cones combined with the addition of nitrogen by laser ablation MC-ICP-MS. *Anal. Chim. Acta* **2016**, *911*, 14–26. [CrossRef] [PubMed]
60. Thompson, J.M.; Meffre, S.; Danyushevsky, L. Impact of air, laser pulse width and fluence on u–pb dating of zircons by LA-ICPMS. *J. Anal. At. Spectrom.* **2018**, *33*, 221–230. [CrossRef]
61. Paton, C.; Woodhead, J.D.; Hellstrom, J.C.; Hergt, J.M.; Greig, A.; Maas, R. Improved laser ablation u-pb zircon geochronology through robust downhole fractionation correction. *Geochem. Geophys. Geosystems* **2010**, *11*, 2009GC002618. [CrossRef]
62. Paul, B.; Petrus, J.; Savard, D.; Woodhead, J.; Hergt, J.; Greig, A.; Paton, C.; Rayner, P. Time resolved trace element calibration strategies for LA-ICP-MS. *J. Anal. At. Spectrom.* **2023**, *38*, 1926–1995. [CrossRef]
63. Mcdowell, F.W.; Mcintosh, W.C.; Farley, K.A. A precise 40ar–39ar reference age for the durango apatite (u–th)/he and fission-track dating standard. *Chem. Geol.* **2005**, *214*, 249–263. [CrossRef]
64. Thomson, S.N.; Gehrels, G.E.; Ruiz, J.; Buchwaldt, R. Routine low-damage apatite u-pb dating using laser ablation–multicollector–ICPMS. *Geochem. Geophys. Geosystems* **2012**, *13*, 2011GC003928. [CrossRef]
65. Rye, R.O.; Ohmoto, H. Sulfur and carbon isotopes and ore genesis: A review. *Econ. Geol. Bull. Soc. Econ. Geol.* **1974**, *69*, 826–842. [CrossRef]
66. Yang, Z.; Huang, Y.; Xu, Z.; Zhao, Y.; Ciren, L.; Zhu, T.; Yuan, K. Textures and trace element geochemistry of pyrite in gaoloushan ore section of the yangshan gold belt, West Qinling: Implications for ore genesis. *Ore Geol. Rev.* **2024**, *165*, 105908. [CrossRef]
67. Machel, H.G. Bacterial and thermochemical sulfate reduction in diagenetic settings—Old and new insights. *Sediment. Geol.* **2001**, *140*, 143–175. [CrossRef]

68. Chang, Z.; Large, R.R.; Maslennikov, V. Sulfur isotopes in sediment-hosted orogenic gold deposits; Evidence for an early timing and a seawater sulfur source. *Geology* **2008**, *36*, 971–974. [CrossRef]
69. Kesler, S.E.; Riciputi, L.C.; Ye, Z. Evidence for a magmatic origin for carlin-type gold deposits: Isotopic composition of sulfur in the betze-post-screamer deposit, nevada, USA. *Miner. Depos.* **2005**, *40*, 127–136. [CrossRef]
70. Bralia, A.; Sabitini, G.; Troja, F. A revaluation of the co/ni ratio in pyrite as geochemical tool in ore genesis problems. *Miner. Depos.* **1979**, *14*, 354–374. [CrossRef]
71. Loftus-Hills, G.; Solomon, M. Cobalt, nickel and selenium in sulphides as indicators of ore genesis. *Miner. Depos.* **1967**, *2*, 228–242. [CrossRef]
72. Cao, G.; Zhang, Y.; Chen, H. Trace elements in pyrite from orogenic gold deposits: Implications for metallogenic mechanism. *Acta Petrol. Sin.* **2023**, *39*, 2330–2346. (In Chinese) [CrossRef]
73. Li, R.; Tan, Q.; Wang, X.; Sun, X.; Yang, T.; Xia, Y.; Guan, Y.; Feng, Y. A metasedimentary origin for gold deposits in the dian-qian-gui "golden triangle" of southwest China. *Ore Geol. Rev.* **2023**, *159*, 105560. [CrossRef]
74. Wang, L.; Chiaradia, M.; Qin, K.; Hui, K.; Li, Z.; Cao, M.; Song, G.; Pang, X.; Shan, P.; Li, G. Magmatic controls on au- and ag-rich intermediate-sulfidation epithermal deposits from northeast China. *Econ. Geol.* **2024**, *119*, 1913–1936. [CrossRef]
75. Hu, X.; Ding, Z.; Gong, Y.; Li, K.; He, M. Sediment-hosted disseminated gold deposits in orogenic belts: An example from the giant jiagantan gold deposit in the West Qinling orogen, China. *Ore Geol. Rev.* **2022**, *146*, 104950. [CrossRef]
76. Large, R.R.; Danyushevsky, L.; Hollit, C.; Maslennikov, V.; Meffre, S.; Gilbert, S.; Bull, S.; Scott, R.; Emsbo, P.; Thomas, H.; et al. Gold and trace element zonation in pyrite using a laser imaging technique; Implications for the timing of gold in orogenic and carlin-style sediment-hosted deposits. *Econ. Geol. Bull. Soc. Econ. Geol.* **2009**, *104*, 635–668. [CrossRef]
77. Deditius, A.P.; Utsunomiya, S.; Renock, D.; Ewing, R.C.; Ramana, C.V.; Becker, U.; Kesler, S.E. A proposed new type of arsenian pyrite: Composition, nanostructure and geological significance. *Geochim. Cosmochim. Acta* **2008**, *72*, 2919–2933. [CrossRef]
78. Phillips, G.N.; Powell, R. Formation of gold deposits: A metamorphic devolatilization model. *J. Metamorph. Geol.* **2010**, *28*, 689–718. [CrossRef]
79. Xue, X.; Feng, Y.; Tamer, M.T.; Liu, T.; Li, K.; Ma, J.; Zhou, J.; Yu, H.; Ding, Z. Comparison of gold precipitation processes between disseminated and quartz vein ores of orogenic gold deposits: Insights from the linglong gold field, Jiaodong Peninsula, China. *Ore Geol. Rev.* **2025**, *183*, 106639. [CrossRef]
80. Groves, D.I.; Goldfarb, R.; Gebre-Mariam, M.; Hagemann, S.G.; Robert, F. Orogenic gold deposits: A proposed classification in the context of their crustal distribution and relationship to other gold deposit types. *Ore Geol. Rev.* **1998**, *13*, 7–27. [CrossRef]
81. Goldfarb, R.J.; Groves, D.I. Orogenic gold: Common or evolving fluid and metal sources through time. *Lithos* **2015**, *233*, 2–26. [CrossRef]
82. Ni, C.; Jiang, Y. Petrogenesis and Tectonic Implications of the Indosinian Fengxian Pluton, Western Qinling Orogeny. *Geol. J. China Univ.* **2023**, *29*, 559–570. (In Chinese)
83. Yu, P.; Li, C.; Fu, J.; Wang, J.; Zhang, J.; Zhang, H.; Ren, H.; Yu, H.; Luo, J.; He, Z.; et al. Laser ablation inductively coupled plasma tandem mass spectrometry (LA-ICP-MS/MS) rb-sr sericite geochronology in orogenic gold deposits: Strategies and significance. *Ore Geol. Rev.* **2025**, *180*, 106543. [CrossRef]
84. Wang, Z.; Liu, J.; Carranza, E.J.M.; Xue, R.; Zhai, D.; Weng, G.; Zhao, Q.; Wang, L.; Wang, G.; Zhang, B. Constraints on the metallogenesis of the liba gold deposit, West Qinling orogen, China: Evidence from rutile u–pb dating, pyrite geochemistry and sulfides in-situ s–pb isotopes. *Ore Geol. Rev.* **2025**, *184*, 106741. [CrossRef]
85. Zeng, Q.; Evans, N.J.; Mcinnes, B.I.A.; Batt, G.E.; Mccuaig, C.T.; Bagas, L.; Tohver, E. Geological and thermochronological studies of the dashui gold deposit, West Qinling orogen, central China. *Miner. Depos.* **2013**, *48*, 397–412. [CrossRef]

Disclaimer/Publisher's Note: The statements, opinions and data contained in all publications are solely those of the individual author(s) and contributor(s) and not of MDPI and/or the editor(s). MDPI and/or the editor(s) disclaim responsibility for any injury to people or property resulting from any ideas, methods, instructions or products referred to in the content.